Ocean Modelling 132 (2018) 112–129

Contents lists available at ScienceDirect

Ocean Modelling

journal homepage: www.elsevier.com/locate/ocemod

# A simplified energetics based planetary boundary layer (ePBL) approach for ocean climate simulations.

Brandon G. Reichl[*,a], Robert Hallberg[b,a]

[a] Program in Atmospheric and Oceanic Sciences, Princeton University, Princeton, NJ, USA
[b] NOAA Geophysical Fluid Dynamics Laboratory, Princeton, NJ, USA

ARTICLE INFO

*Keywords:*
Vertical mixing
Parameterization
Upper ocean
Turbulent boundary layer

ABSTRACT

This paper presents a method to parameterize vertical turbulent mixing coefficients within the ocean surface boundary layer (OSBL) for climate applications. The new method is specifically constructed to satisfy two requirements. The first aspect is to explicitly consider the mechanical energy budget of the turbulence that drives mixing. This constraint ensures a realistic and robust simulation of the OSBL, which is critical for coupled climate simulations. The second aspect is that the model should be formulated so that it is not sensitive to the numerical limitations common to climate simulations, such as long time-steps and coarse vertical grids. This goal is achieved by combining an existing resolved shear-driven mixing parameterization (here Jackson et al., 2008) with a new method to avoid time step sensitivity. The new method is motivated by the Kraus-Turner-Niiler type bulk boundary layer parameterization, but relaxes the requirement for vertical homogeneity. The non-dimensional coefficients $m_*$ and $n_*$ from the Kraus-Turner-Niiler approach are parameterized for the new method based on results of simulations using a previously tested parameterization at high resolution. The resulting parameterization is evaluated by comparing simulations with the new parameterization to simulations with the $k-\epsilon$ parameterization over a wide range of combinations of surface wind stress, surface buoyancy flux, and latitudes. The new method for vertical turbulent OSBL mixing is therefore proposed as a computationally efficient, implicitly energetically constrained option appropriate for ocean climate modeling applications.

## 1. Introduction

The ocean surface boundary layer (OSBL) is the only part of the ocean directly influenced by the atmosphere. It is also a region where turbulent energy and dissipation often exceeds the ocean interior values by several orders of magnitude. This elevated turbulence leads to a fundamentally unique regime where distinct physical processes govern the dynamics compared to the interior (e.g. Moum and Smyth, 2001; Soloviev and Lukas, 2013). The OSBL is bounded at its surface by the air-sea interface, while the bottom boundary is typically constrained by strong density gradients. The vigorous turbulence results in significant mixing within this layer, combining properties modified by the atmosphere above and entrainment from the ocean interior below.

The physics that govern this regime couple processes spanning from the small scale of dissipation to eddies as large as the boundary layer. For simulating large-scale ocean climate, current computational allocations dictate the use of hydrostatic momentum equations discretized with horizontal grid spacing between 25–100 km and variable vertical grid spacing between 1–100 m (e.g. Griffies et al., 2016). The vertical grid spacing may be finest within the boundary layers to resolve important near-surface processes and coarsest in the interior. This grid does not resolve OSBL turbulence, requiring the effect of turbulence on ocean evolution to be simulated using boundary layer parameterization.

### 1.1. Boundary layer parameterizations

The leading-order mean OSBL equation for arbitrary scalar $\phi$ assuming a horizontally homogenous distribution is:

$$\frac{\partial\bar{\phi}}{\partial t} = -\frac{\partial}{\partial z}\overline{w'\phi'} + \nu_\phi\frac{\partial^2\bar{\phi}}{\partial z^2}, \tag{1}$$

where $\nu_\phi$ is the molecular diffusivity, $w$ is the vertical velocity, and $w'$ and $\phi'$ are fluctuations from ensemble averages $\bar{w}$ and $\bar{\phi}$. This equation describes the evolution of mean quantity $\bar{\phi}$ due to vertical processes, including the divergence of the turbulent flux (covariance) term and often negligible molecular mixing. A challenge common to simulating any turbulent fluid at resolutions coarser than those required for DNS

* Corresponding author.
*E-mail addresses:* breichl@princeton.edu, brandon.reichl@noaa.gov (B.G. Reichl).

https://doi.org/10.1016/j.ocemod.2018.10.004
Received 4 April 2018; Received in revised form 24 September 2018; Accepted 11 October 2018
Available online 12 October 2018

(Direct Numerical Simulation, where turbulent fluxes are entirely resolved) is to skillfully parameterize the turbulent fluxes (*the turbulence-closure problem*). For practical oceanographic applications this parameterization must emphasize computational efficiency.

There is a wide-range of approaches that are employed to parameterize turbulent fluxes for ocean simulations (see Burchard et al., 2008). Here we focus on energetics based OSBL parameterizations. The downward turbulent flux of buoyant water by OSBL turbulence converts mechanical energy into potential energy as it mixes with less buoyant water at the base of the OSBL. We focus on OSBL parameterizations that constrain this integrated potential energy conversion due to turbulent mixing.

A simple method employed by several older-generation basin and global scale ocean models is the Kraus-Turner-Niiler well-mixed boundary layer parameterization (Kraus and Turner, 1967; Niiler and Kraus, 1977). The Kraus-Turner-Niiler method assumes no vertical property gradients inside a well-mixed OSBL. The relative simplicity of this approach facilitates implementation of exact implicit solvers for the potential energy change due to turbulent mixing in the water column. Simulations employing this scheme are therefore not significantly degraded by coarse vertical resolution and long time-steps.

Another approach follows the Boussinesq hypothesis (Boussinesq, 1877) for turbulence closure. This hypothesis approximates the Reynolds stress terms using an eddy viscosity (eddy diffusivity for turbulent scalar fluxes)[1]. The Reynolds stress is parameterized as down-gradient of the mean velocity profile (as an analogue to molecular viscosity):

$$\overline{u_i' w'} = -K_M \frac{\partial \bar{u}_i}{\partial z}, \tag{2}$$

where $u_i$ are the horizontal components of the velocity. Similarly, the eddy diffusivity is used to parameterize turbulent scalar fluxes as:

$$\overline{\phi' w'} = -K_\phi \frac{\partial \bar{\phi}}{\partial z}. \tag{3}$$

The parameters needed to close the system of equations are then reduced to the turbulent mixing coefficients, $K_\phi$ and $K_M$. First-order approaches determine these coefficients based on mean flow parameters, such as in the K-Profile Parameterization (KPP, Large et al., 1994) and Pacanowski and Philander (1981). However, first-order approaches do not typically consider the change of the potential energy in the water column due to turbulent mixing.

Second-order[2] parameterizations formulate equations to predict the mixing coefficients using second-moment turbulent quantities such as the turbulent kinetic energy (TKE). These approaches explicitly consider energetic constraints of turbulent mixing via the mechanical TKE conservation equation (discussed further in Section 2.2). The most complex approaches of this nature are based on a consistent mathematical framework to express the coupled differential equations for the turbulent fluxes. These approaches are summarized by the systematic "level of closure" description proposed by Mellor and Yamada (1974) (see also Galperin et al., 1988; Canuto et al., 2001). Several types of second-order turbulent closure have been applied to oceanic boundary layers, most notably Mellor-Yamada ($k-kl$, see Mellor and Yamada (1982), Kantha and Clayson (1994), and Canuto et al. (2001)), $k-\epsilon$ (e.g. Rodi (1987) and Burchard and Baumert (1995)), $k-\omega$ (e.g. Wilcox (1988) and Umlauf and Burchard (2003)), and the Generic Length Scale (GLS) (e.g. Umlauf and Burchard (2003) and Kantha (2004)).

For climate simulation there are computational challenges that discourage use of second-order OSBL parameterization. Second-order approaches are most-often employed for coastal ocean models, where numerical stability restrictions (with horizontal grid spacing less than 1 km) dictate model time-steps on the order of minutes for the dynamics, which approximately corresponds to timescales of turbulence evolution. Global models with a grid spacing of 25 km or more permit dynamics time-steps greater than 1000 s and thermodynamic (mixing) time-steps exceeding one hour. The large time-steps limit the use of the second-order approach in global models, since the timescales of TKE evolution are unresolved (see Reffray et al., 2015).

Boundary layer parameterizations that require short time-steps in ocean models make the resultant model impractical for studying climate timescale phenomenon. Several approximations and simplifications have been proposed to ease the computational burden associated with second-order methods (see Gaspar et al., 1990; D'Alessio et al., 1998). However, these models remain sensitive to the time-step due to the coupled evolution of the turbulence and the mean fields (see Reffray et al., 2015). One second-order method we will discuss further in Section 2.3 is specifically formulated to employ in climate models (Jackson et al., 2008, hereafter JHL). JHL has not previously been implemented for turbulent mixing in the OSBL.

Surface waves are known to significantly impact the dynamics of the OSBL (Belcher et al., 2012; D'Asaro et al., 2014). Recent studies have demonstrated the importance of wave effects to improve biases in ocean mixing in climate models (Fan and Griffies, 2014; Li et al., 2016). These studies both employed the first-order KPP parameterization modified to include the effect of surface waves. For brevity, we reserve discussion of parameterization of the effect of waves within climate models for a separate study. The limitations of neglecting wave effects are discussed further in Section 6.1.

### 1.2. Outline

We present here a framework to parameterize OSBL turbulent mixing for climate models. Our approach is motivated to satisfy two criteria. First, it must maintain a realistic constraint on potential energy change due to turbulent mixing in the OSBL. Second, the computational requirement of the parameterization must be low relative to other components of the ocean model. Moreover, it must accurately represent the effects of turbulence in models that operate with the time-step that characterizes the dynamics of the ocean-climate system (about one hour).

We begin (Section 2) with a review of mechanical energy based OSBL parameterizations. We demonstrate that the well-mixed boundary layer framework is skillful for limiting sensitivity of OSBL parameterization to time-step and vertical resolution. In Section 3 we investigate the energetic constraints imposed in the well-mixed boundary layer formulation. In Section 4 we describe a new method to extend the well-mixed boundary layer parameterization to simulations that do not require a homogenous OSBL. Finally, in Section 5 the capabilities of this method are tested against a commonly used second-order turbulent mixing parameterization run with fine vertical resolution and small time-step (the $k-\epsilon$ parameterization with Schumann and Gerz (1995) stability functions). The result of this study is the formulation of a simplified implicit energetics based method to parameterize the effects of turbulence in the ocean surface boundary layer that can be implemented with minimal computational overhead and minimal resolution sensitivity for coupled ocean-climate simulations.

## 2. Energetically constrained OSBL parameterizations for climate models

The energetics of OSBL turbulence are described by the mechanical TKE conservation equation (see Rodi, 1987):

[1] See Schmitt (2007) for discussion on the historical connection between J. Boussinesq's hypothesis and O. Reynold's work.

[2] Here we adopt the colloquial terminology of "order" that is common in the literature, though formally these parameterizations are referred to by their "moment".

$$\frac{\partial k}{\partial t} = \frac{\partial}{\partial z}\left(\frac{K_M}{\sigma_k}\frac{\partial k}{\partial z}\right) - u_i'w'\frac{\partial \bar{u}_i}{\partial z} + w'b' - \epsilon, \tag{4}$$

where $k$ is the TKE, $\sigma_k$ is the turbulent Schmidt number, $b$ is the buoyancy, and $\epsilon$ is the turbulent dissipation rate. The terms in this equation represent TKE storage (LHS), TKE flux convergence (RHS, 1st), shear production (RHS, 2nd), buoyancy production (RHS, 3rd), and dissipation (RHS, 4th). The term that contributes to potential energy conversion is the buoyancy production term.

We review three types of energetically constrained mixing parameterizations in this section that consider the effect of this buoyancy term on ocean energetics. We start by reviewing the well-mixed boundary layer approach (Section 2.1). This approach integrates the OSBL and applies Eq. (4) to predict an entrainment velocity. Second, we review approaches that solve Eq. (4) and use the TKE to constrain the turbulent mixing (Section 2.2). Finally, we review another method based on Eq. (4), but that makes simplifications targeted for implementation in climate model configurations (Section 2.3).

We restrict discussion in this section to schemes that are energetically constrained. Therefore, first-order parameterizations such as KPP (Large et al., 1994) are not discussed in detail. These parameterizations use energetically motivated Richardson number arguments to predict the mixing coefficients. However, they do not explicitly consider the effect of the mixing coefficient on the potential energy conversion in the water column.

### 2.1. Well-Mixed boundary layers (WMBLs)

The well-mixed boundary layer (WMBL) parameterization[3] is described in detail in several previous studies (see Kraus and Turner, 1967; Niiler and Kraus, 1977; Garwood, 1977; Deardorff, 1983; Gaspar, 1988; Oberhuber, 1993). WMBLs assume that the OSBL is vertically homogeneous, which simplifies the ocean model by simulating only vertical integrals within the OSBL. The integral of Eq. (1) for $\bar{\phi}$ over the OSBL thickness ($H_{bl}$) is:

$$\int_{-H_{bl}}^{0} \frac{\partial \bar{\phi}}{\partial t} dz = -\int_{-H_{bl}}^{0} \frac{\partial}{\partial z}(\overline{\phi' w'}) dz, \tag{5}$$

where ensemble averages are assumed ($\overline{\phi' w'}$) and the molecular component is assumed small (large Reynolds number). The quantity $\bar{\phi}$ is assumed uniform in this layer, so Eq. (5) is written (e.g. Gaspar, 1988):

$$\frac{\partial \langle \bar{\phi} \rangle}{\partial t} = -\frac{1}{H_{bl}}[\overline{\phi' w'}_0 - \overline{\phi' w'}_{bl}], \tag{6}$$

where $\langle \quad \rangle$ denotes a vertically averaged quantity.

The turbulent boundary-conditions are the only turbulence quantities retained in (6). The prescribed surface flux arises from air-sea and ice-sea exchange of matter, energy, and momentum. The bottom turbulent entrainment flux in WMBLs are written in jump-form (following Niiler and Kraus, 1977):

$$\overline{\phi' w'}_{bl} = -w_e(\langle \bar{\phi} \rangle - \bar{\phi}_I) = -w_e \Delta \bar{\phi}, \tag{7}$$

where $\phi_I$ is the interior value of $\phi$ and $w_e$ is the entrainment velocity. The entrainment velocity is the only turbulent quantity requiring closure in WMBLs. This term is the time derivative of the OSBL depth (Gaspar, 1988):

$$w_e = \partial H_{bl}/\partial t \quad \partial H_{bl}/\partial t > 0 \tag{8a}$$

$$w_e = 0 \quad \partial H_{bl}/\partial t < = 0. \tag{8b}$$

In WMBLs the TKE (4) is assumed steady-state and is integrated over the OSBL (following Niiler and Kraus, 1977):

$$0 = \int_{-H_{bl}}^{0} \frac{\partial}{\partial z}\left(\frac{K_M}{\sigma_k}\frac{\partial k}{\partial z}\right) dz - \int_{-H_{bl}}^{0} u_i'w'\frac{\partial \bar{u}_i}{\partial z} dz + \int_{-H_{bl}}^{0} w'b' dz - \int_{-H_{bl}}^{0} \epsilon dz. \tag{9}$$

The terms of Eq. (9) are parameterized to determine $w_e$ (following Niiler and Kraus, 1977; Gaspar, 1988). The first RHS term (TKE flux convergence) is parameterized as $m_2 u_*^3$ . This proportionality assumes the surface TKE flux is correlated to the friction velocity cubed ($u_* = (|\tau|/\rho_0)^{1/2}$, $\tau$ is the wind stress) via a coefficient, $m_2$. This surface TKE flux could represent (for example) TKE injection by breaking surface waves. The second RHS term (TKE shear production) is parameterized as $m_3 u_*^3$. The third RHS term (buoyancy production) is known for a uniform well-mixed layer as:

$$\int_{-H_{bl}}^{0} w'b' dz = -\frac{1}{2} H_{bl} w_e \Delta b - \frac{1}{2} H_{bl} B(H_{bl}), \tag{10}$$

where $B(H_{bl})$ is the surface buoyancy flux considering interfacial and penetrative (short-wave) fluxes. Both RHS terms in Eq. (10) can contribute to increased potential energy through turbulent mixing. The first term increases potential energy when the OSBL deepens ($w_e > 0$). The second RHS term accounts for potential energy change by turbulent mixing in the presence of stabilizing surface fluxes.

The final term in Eq. (9) is the dissipation. One simple option to parameterize dissipation assumes that it is proportional to production via a convective proportionality coefficient ($1 - n_*$) and a mechanical proportionality coefficient ($m_d$) (Niiler and Kraus, 1977; Gaspar, 1988):

$$\int_{H_{bl}}^{0} \epsilon dz = m_d u_*^3 + \frac{H_{bl}}{2}(1 - n_*) B(H_{bl}). \tag{11}$$

During stabilizing surface buoyancy flux $n_*$ is unity, and it becomes less than one during convection (this study discusses the proper value in Section 3.1).

Following the assumptions above, the boundary layer TKE balance is:

$$\frac{1}{2} H_{bl} w_e \Delta b = m_* u_*^3 - n_* \frac{H_{bl}}{2} B(H_{bl}), \tag{12}$$

where the sum of the mechanical $m$ coefficients is defined as:

$$m_* = m_2 + m_3 - m_d. \tag{13}$$

The first RHS term ($m_* u_*^3$) in Eq. (12) represents the increase of water column potential energy by mechanically produced TKE. In the presence of a stabilizing surface flux this term must exceed the surface buoyancy flux term for $w_e$ to be non-zero. The second RHS term in Eq. (12) contributes to $w_e$ during destabilizing surface buoyancy fluxes. When there is sufficient TKE produced by the wind, waves, and convection to counter the TKE destroyed by dissipation (and mixing of surface stratification associated with a stabilizing surface flux), then the boundary layer deepens. When the TKE production is no longer greater than dissipation, the LHS of Eq. (12) is taken to be zero and the boundary layer depth retreats to the Monin-Obhukov depth ($\propto -u_*^3/\overline{w'b'}_0$). The stabilizing-rotational OSBL depth limit of Zilitinkevich and Mironov (1996) indicates that the value of $m_*$ should depend also on Coriolis parameter $|f|$ in this limit. Oberhuber (1993) indeed include additional vertical dissipation to $m_*$ exponentially dependent on the Ekman length ($\propto \exp[z|f|/u_*]$). We investigate implications of rotation in WMBLs in further detail in Section 3.2. For discussion of traditional values of $n_*$ and $m_*$ see Gaspar (1988).

In prior generations of large-scale ocean models, the cheap computational cost of implementing Eq. (12) motivated use of WMBLs (e.g. Oberhuber, 1993; Bleck, 2002; Thompson et al., 2002). Furthermore, the total energy available for entrainment is prescribed from $m_*$ and $n_*$ and therefore is not sensitive to model time-step and vertical resolution. However, there are well-known limitations for climate models to assume that quantities are vertically uniform within the OSBL. For example, the structure of the Ekman spiral is important for restratification of the OSBL along horizontal density gradients (e.g. Rodhe, 1991;

[3] Historically these are often called “mixed layer” or “bulk mixed layer” parameterization. We prefer “well-mixed boundary layer” to be consistent with parameterizations that do not require a vertically homogenous OSBL.

Thomas and Ferrari, 2008; D'Asaro et al., 2011).

### 2.2. Second-Order TKE parameterizations

In second-order $K$-parameterizations, the mixing coefficients (Eqs. (2) and (3)) are predicted from dimensional reasoning (as an analogue to the kinetic theory of gas):

$$K_M = c_\mu k^{1/2} l \tag{14a}$$

$$K_\phi = c'_\mu k^{1/2} l, \tag{14b}$$

where $c_\mu$ and $c'_\mu$ are stability functions (the ratio of the two is the turbulent Prandtl number, $Pr$) and $l$ is a turbulent length scale.

The TKE Eq. (4) is solved numerically in second-order parameterizations. The dissipation term ($\epsilon$) is dimensionally related to the length scale and the TKE via (Kolmogorov, 1942):

$$\epsilon = (c^0_\mu)^3 \frac{k^{3/2}}{l}, \tag{15}$$

where $c^0_\mu$ is a model coefficient linking the turbulent length scale to the TKE and the dissipation. Simplified one-equation and two-equation methods parameterize the stability functions from mean quantities. The length-scale is typically modeled using either a second prognostic equation (such as in 'two-equation' models, e.g., $k-\epsilon$ (Rodi, 1987; Burchard and Baumert, 1995), $k-kl$ (Mellor and Yamada, 1982; Galperin et al., 1988; Canuto et al., 2001), $k-\omega$ (Wilcox, 1988; Umlauf and Burchard, 2003), and GLS (Umlauf and Burchard, 2003; Kantha, 2004)) or an algebraic relationship (such as in 'one-equation' models, e.g., $k-l$ (Gaspar et al., 1990)).

In the two-equation $k-\epsilon$ closure the $\epsilon$ (dissipation) equation is solved prognostically from (see Rodi, 1987):

$$\frac{\partial \epsilon}{\partial t} = \frac{\partial}{\partial z}\left(\frac{K_M}{\sigma_\epsilon}\frac{\partial \epsilon}{\partial z}\right) + \frac{\epsilon}{k}(c_{1\epsilon} K_M S^2 - c_{3\epsilon} K_\phi N^2 - c_{2\epsilon}\epsilon), \tag{16}$$

where $S^2$ is the shear-squared, $N^2$ is the buoyancy frequency, and the coefficients $c_{n\epsilon}$ parameterize processes relevant to the evolution of dissipation (see Umlauf and Burchard, 2005). The relationship between these coefficients determines the steady-state Richardson number of the parameterization, which is critical for determining the entrainment rate in any second-order model (Burchard and Baumert, 1995). The alternative prognostic length-scale approaches have relatively similar forms (c.f. Rodi, 1987; Umlauf and Burchard, 2003; Kantha, 2004) and give consistent results if the empirical coefficients are adjusted accordingly (Rodi, 1987; Burchard et al., 1998; Burchard and Bolding, 2001; Warner et al., 2005). One-equation approaches simplify the implementation to estimate the length scale from algebraic relationships. In many scenarios one-equation methods provide reasonable estimates for the turbulent mixing (Reffray et al., 2015).

An empirical approach to determine stability functions is to approximate them as functions of quantities such as the gradient Richardson number, $Ri_g$. This approach assumes relationships between the Prandtl number and the Richardson number (Schumann and Gerz, 1995; Peters and Baumert, 2007; Ilıcak et al., 2008).

### 2.3. A two-equation closure for climate models by Jackson et al. (2008)

The two-equation $K$ parameterization of Jackson et al. (2008) was developed for parameterizing mixing due to internal shear layers in the ocean, such as in the Equatorial under-current or in deep-ocean density overflows. Here we apply this parameterization for OSBL wind-driven shear turbulence. While the equations of JHL formally include both convective and shear sources of TKE, it is only previously calibrated for parameterization of shear turbulence. We therefore limit discussion of this parameterization to shear-driven turbulence.

The JHL approach simplifies the two-equation framework to facilitate fully implicit numerics for climate models. The TKE conservation equation is found from Eq. (4) with steady-state and assumed dissipation functions:

$$0 = \frac{\partial}{\partial z}\left(\frac{K_M}{\sigma_k}\frac{\partial k}{\partial z}\right) + K_M S^2 - K_\phi N^2 - k(c_N N + C_M S), \tag{17}$$

where $C_N$ and $C_M$ are empirical model dissipation coefficients. The second (length-scale) equation in JHL is a steady-state conservation equation for the diffusivity itself, $K \propto k^{1/2} l$, due to turbulent flux, a production (source), and two dissipation (sink) terms (see Jackson et al., 2008; Umlauf, 2009):

$$0 = \frac{\partial}{\partial z}\left(K\frac{\partial K}{\partial z}\right) + 2KSF^* - \frac{K}{L_d^2} - \left(\frac{\partial K}{\partial z}\right)^2 \tag{18}$$

where $L_d$ is a turbulent length scale and $F^*$ is an empirical function (following Ellison and Turner, 1959):

$$F^* = F_0\left(\frac{1 - Ri_g/Ri_c}{1 + \alpha^* Ri_g/Ri_c}\right), \tag{19}$$

where $Ri_g = N^2/S^2$ is the gradient Richardson number, $Ri_c$ is the critical Richardson number, and $F_0$ and $\alpha^*$ are model coefficients. In JHL, Eq. (18) is presented in equivalent, alternative form as:

$$\frac{K}{L_d^2} - \frac{\partial^2 K}{\partial z^2} = 2KSF^* \tag{20}$$

We do not distinguish between $K_\phi$ and $K_M$ here, implying a Prandtl number of unity, though more general approaches apply.

Umlauf (2009) discusses the physical implications of JHL in reference to more traditional second-order methods. The assumptions involved in using Eqs. (17) and (20) facilitate implementation of coupled, cost-effective, iterative implicit numerical solvers for both the turbulent properties and their impacts on the momentum and density structure (see JHL). This fully implicit approach facilitates parameterizing shear-driven turbulent mixing in models with time-steps characteristic of climate simulations (e.g., within MOM6 climate model configurations, Adcroft et al., in prep).

### 2.4. Considerations for global climate model time-steps and vertical resolution

In this section three energetically based OSBL turbulent mixing parameterizations were discussed. There are two aspects of such parameterizations that we consider for implementation in a global ocean model. First is the ability of the parameterization to accurately simulate boundary layer physics. Second is the ability of the parameterization to work in computationally restricted numerical implementations including coarse vertical resolution and long time-steps. To evaluate the ability of the three parameterizations to work well with coarse vertical resolution and long time-steps, we investigate results from simulations of one-dimensional column models with various time-steps and resolutions (see Appendix B for details on the one-dimensional model implementations). To test the sensitivity to vertical resolution we vary the model grid thickness using values of 1, 5, 10, and 20 m, with a constant time-step of 10 s. To test the sensitivity to time-step we vary the model time-step from 1 s to 7200 s, with a constant grid thickness of 1 m. We will examine the performance of the OSBL parameterizations in both wind-shear driven and buoyancy driven turbulence conditions.

For this exercise we use the $k-\epsilon$ parameterization with the Schumann and Gerz (1995) stability functions as our two-equation $K$ parameterization (hereafter $k-\epsilon$-SG). The $k-\epsilon$-SG parameterization chosen here has previously been validated by observational studies (Peters and Baumert, 2007; Ilıcak et al., 2008). We also include results from a WMBL parameterization with constant $m_* = 1.2$ and $n_* = 0.2$. For the shear-driven case we also include simulations using the JHL parameterization.

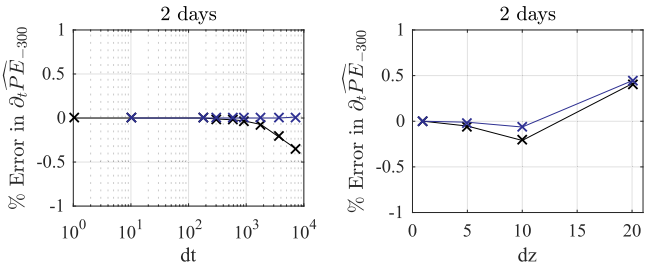


**Fig. 1.** Effect of time-step (left) and vertical grid spacing (right) on simulated integrated Potential Energy change in simulations with the bulk mixed layer (blue) and $k-\epsilon$-SG (black) for simulations with $-100\,\mathrm{W\,m^{-2}}$ of cooling. The % error is relative to the smallest time-step (left) or dz (right) for a given parameterization. The $\wedge$ notation represents vertically integrated potential energy (the subscript denotes that the integral is over the upper 300 m). (For interpretation of the references to colour in this figure legend, the reader is referred to the web version of this article.)

To evaluate the effect of resolution on the energetic constraint we investigate the change in integrated potential energy. We initialize the model with a constant temperature gradient ($0.01\,^{\circ}\mathrm{C\,m^{-1}}$) and homogenous salinity. In each case the integrated temperature is consistent between all runs, but the vertical distribution of this temperature changes the potential energy. The change in potential energy is due to both the application of a surface heat flux and the entrainment/mixing. The surface flux contribution is unrelated to the turbulence parameterization and both are sensitive to the vertical resolution. In all cases results are presented after 48 hours of simulation.

### 2.4.1. One-Dimensional simulation of convective OSBL

First, we investigate a case where the turbulent mixing is driven by convection via cooling of $-100\,\mathrm{W\,m^{-2}}$. We find that both the WMBL and the $k-\epsilon$-SG turbulence models give little sensitivity to time-step and vertical resolution after 2 simulation days (Fig. 1). The vertical resolution sensitivity is related to the coarseness of the first model layer, where the surface cooling is applied evenly over 1, 5, 10, or 20 m depending on the resolution. Note that the non-monotonic behavior with thickness is variable in time, indicating the complex relationship between potential energy change due to surface cooling and entrainment.

### 2.4.2. One-Dimensional Simulation of Wind-Driven OSBL

Next we simulate a case with a strong surface wind forcing of $1\,\mathrm{N\,m^{-2}}$. In this case, rotation effects are important for the boundary layer so we include both a case with no rotation (Equatorial) and a case with maximum rotation (North Pole). We find that with no rotation the $k-\epsilon$-SG model gives significant sensitivity to long time-steps, missing all mixing at 7200 s (Fig. 2). The JHL approach does not show this dependency, likely because JHL is implemented in the model fully implicitly over the coupled turbulence and mean-flow evolution, whereas the $k-\epsilon$-SG implementation solves the TKE and $\epsilon$ implicitly dependent on the previous time-step mean parameters.

At high-latitudes both the JHL model and the $k-\epsilon$-SG model are sensitive to the time-step and the grid spacing. The effect of rotation is not directly considered within any equations of the two-equation OSBL parameterization. The effect of rotation on the column model is therefore entirely due to its effect on the evolution of the mean horizontal current profile. This feeds-back to the turbulence through the mean-shear profile, which will affect both the shear-production term and the dissipation equation. The sensitivity to grid spacing is therefore likely due to limited ability to resolve the temporal and spatial Ekman spiral characteristics at coarse vertical resolution and long time-steps. This is exacerbated by the steady-state equations used in JHL.

The sensitivity to time-step in JHL and $k-\epsilon$-SG is not entirely by the same cause. The $k-\epsilon$-SG sensitivity is likely related to the same

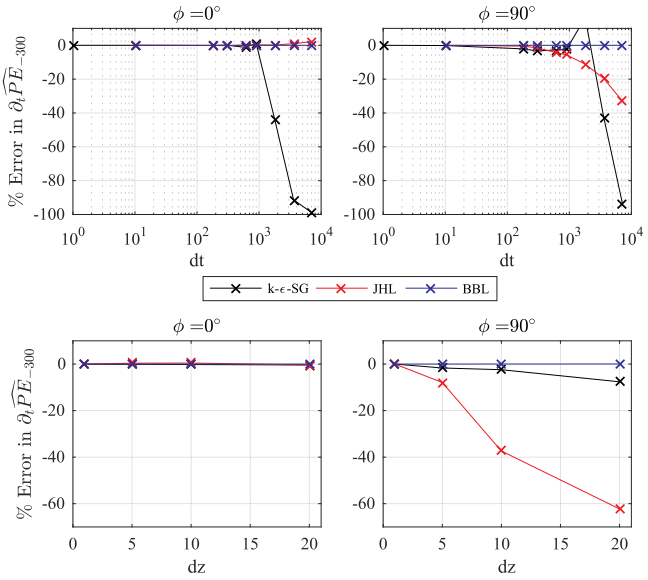


**Fig. 2.** Effect of time-step (top) and vertical grid spacing (bottom) on simulated integrated Potential Energy change in simulations with the bulk boundary layer (blue), $k-\epsilon$-SG (black), and JHL (red) for simulations with $1\,\mathrm{N\,m^{-2}}$ of wind stress. Results given for non-rotating (left) and $f = 1.454\mathrm{e}{-4}\,\mathrm{s^{-1}}$ (right). % error is relative to the smallest time-step (dz in bottom panels) for a given parameterization. The $\wedge$ notation represents vertically integrated potential energy (the subscript denotes that the integral is over the upper 300 m). (For interpretation of the references to colour in this figure legend, the reader is referred to the web version of this article.)

time-step effect that was found at the equator. The JHL scheme was not sensitive to time-step at the equator, so it is likely only affected by time-step due to coupling of turbulence with explicit numerics for Coriolis acceleration. The JHL model is formulated for coupled-implicit turbulence and diffusion numerics, so the time-step dependence at high latitudes shows that significant error may still occur due to a rotating mean flow at long time-steps. In all cases, reduced resolution and longer time-steps both contribute to under-estimated mixing (except at 1200 s in $k-\epsilon$-SG where the model appears to exhibit unstable behavior). The bulk boundary layer has no dependence on vertical resolution or time-step since the total mixing is only constrained by fixed constant external parameters $m_*$ and $u_*$.

### 2.4.3. Implications of numerical sensitivity

This numerical sensitivity experiment does not evaluate the performance of any parameterization to simulate accurate boundary layer physics. The WMBL parameterization (Section 2.1) is not a useful approach for modern climate models because it does not resolve boundary layer structure and relies on poorly constrained global $m_*$ and $n_*$ coefficients. These weaknesses can result in significant biases in prediction of the OSBL evolution. The shear-driven mixing predicted by second-order models is degraded by long time-steps and coarse vertical model resolution, a problematic weakness for ocean climate modeling. The remainder of this manuscript therefore presents a framework motivated to combine the ideas of the WMBL and the $K$ parameterization for an OSBL parameterization capable of consistent turbulent mixing at long time-step and coarse resolution for climate simulations.

## 3. Parameterizations for $m_*$ and $n_*$ based on $k-\epsilon$

The potential energy change by turbulent mixing (hereafter $M$) is computed from the integral of the stabilizing buoyancy flux:

$$\hat{M}_{H_{bl}} = \int_{H_{bl}}^{0} K_{\phi} \max(N^2, 0)\, dz. \tag{21}$$

The $\wedge$ notation represents vertically integrated quantities (the subscript

denotes that the integral is over the OSBL). This quantity has mks units of $[\mathrm{m}^3\ \mathrm{s}^{-3} = (\mathrm{W}\cdot\mathrm{m}^{-2})(\mathrm{m}^3\cdot\mathrm{kg}^{-1})]$, which is the rate of Potential Energy density production per unit horizontal area. In second-order closures (Sections 2.2), this term is a component of the integral balance with the shear production, convective production, dissipation, and TKE storage.

By using (21), we express Eq. (9) of WMBLs as:

$$\hat{M}_{H_{bl}} = \int_{-H_{bl}}^{0} \frac{\partial}{\partial z}\left(\frac{K_M}{\sigma_k}\frac{\partial k}{\partial z}\right)dz + \int_{-H_{bl}}^{0} K_M S^2 dz - \int_{-H_{bl}}^{0} K_\phi \min(N^2, 0)dz - \int_{-H_{bl}}^{0} \epsilon dz. \quad (22)$$

If we follow the WMBL assumption that dissipation is proportional to production via coefficients $m_*$ and $n_*$ (Section 2.1), the RHS of Eq. (22) becomes:

$$\hat{M}_{H_{bl}} = m_* u_*^3 - n_* \int_{-H_{bl}}^{0} K_\phi \min(N^2, 0)dz. \quad (23)$$

The difference in Eq. (23) compared to Eq. (12) is that mixing occurs throughout the OSBL instead of at the base of a homogeneous layer. In this section we investigate precise values of $m_*$ and $n_*$ from this equation, which are equivalent to the $m_*$ and $n_*$ integral constraints of WMBLs.

### 3.1. $n_*$ in convectively forced OSBLs

The freely convecting planetary boundary layer is well-studied previously using observations of the atmospheric boundary layer and LES models. The atmospheric observations show that the entrainment buoyancy flux is about 20% of the destabilizing surface buoyancy flux (e.g. Carson, 1973; Caughey and Palmer, 1979). A LES study for the ocean boundary layer also found this ratio is approximately 20% (Noh et al., 2010). It is important to distinguish that $n_*$ is not this ratio of the surface to the entrainment flux (and not 20%), but rather $n_*$ is the ratio of the integrated positive to the integrated negative buoyancy flux within the OSBL. We use this empirical relation to estimate $n_*$ in Section 3.1.1.

In the case of convection with no mechanical forcing, Eq. (23) simplifies to:

$$\hat{M}_{H_{bl}} = -n_* \int_{-H_{bl}}^{0} K_\phi \min(N^2, 0)dz. \quad (24)$$

This relationship may be employed to estimate $n_*$ from models that solve complete TKE balance equations to predict $K_\phi$ (such as described by Section 2.2). We use this approach to estimate $n_*$ in Section 3.1.2.

#### 3.1.1. $n_*$ Estimated from historical observations

In this section we use the empirical entrainment result to estimate $n_*$. Fig. 3 is a schematic representation from atmospheric convection observations (based on Caughey and Palmer, 1979, their Figure 3), where we invert their figure for the ocean. The buoyancy flux profile decays linearly from the surface value to the entrainment depth. In Fig. 3, the value $H_G$ represents the level where the buoyancy gradient changes sign. Below this depth, denser water is entrained as the boundary layer expands.

The observations show that the entraining buoyancy flux peak is approximately 20% of the surface forcing ($B_f$) (Stull, 1976; Caughey and Palmer, 1979). We infer that the depth of this peak must be about $1.2 \times H_G$, since the flux profile is approximately linear. The areas of the triangles in this representation are the integrated buoyant production (area $A_G$) and integrated mixing ($\hat{M}_{H_{bl}}$, area $A_{M1} + A_{M2}$). If we compute the area of $A_G$ using the height ($H_G$) and the surface flux ($\overline{w'b'}_0$), we find an expression for the buoyant production:

$$A_G = \frac{1}{2}\overline{w'b'}_0 H_G. \quad (25)$$

We compute the area $A_{M1}$ using 20% of the surface flux and 20% of the vertical extent:

$$A_{M1} = \frac{1}{2}(0.2 \times \overline{w'b'}_0)(0.2 \times H_G). \quad (26)$$

There is also entrainment below the entrainment flux peak as it decays toward zero at the OSBL base. This entrainment region is labeled $A_{M2}$ in Fig. 3. We assume that $A_{M2} \geq 0$ and $A_{M2} \leq A_{M1}$. We can thus estimate $n_*$ is $0.04 \leq n_* \leq 0.08$ from:

$$n_* = \frac{\hat{M}_{H_{bl}}}{A_G} = \frac{(A_{M1} + A_{M2})}{A_G}. \quad (27)$$

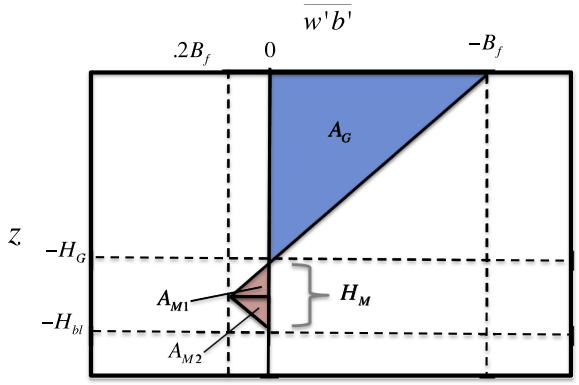


**Fig. 3.** Schematic used to derive the ratio of the TKE production to the TKE converted to potential energy due to a convective surface buoyancy flux (where convention dictates that $B_f = -\overline{w'b'}_0 < 0$ represents buoyancy loss at the ocean surface and $\overline{w'b'} > 0$ is a downward flux of negative buoyancy anomaly). The empirical law of 20% buoyancy flux over 20% of the vertical distance is invoked to facilitate this derivation and is demonstrated here. This buoyancy flux profile is a simplification modeled after the atmospheric equivalent observations presented in Caughey and Palmer (1979).

#### 3.1.2. Computing $n_*$ from $k - \epsilon$

We now estimate $n_*$ from one-dimensional simulations using $k - \epsilon$ with Schumann and Gerz (1995) stability functions (see Appendix B for model details). We simulate the one-dimensional model with various destabilizing heat fluxes and find $n_*$ (from Eq. (24)) is nearly constant (Fig. 4). We estimate $n_* \approx 0.066$ for the range of heat fluxes simulated here, which is within the estimated range from the observations. We compare our estimate for the $n_*$ parameter directly to $b_1$ of Stull (1976) through $n_* = 1 - b_1$. Using the symbols from their study, $A_1$ is between 10 and 30% and $b_1 = 1 - A_1^2$ is between 0.91 and 0.99. Therefore, $n_*$ inferred from their study is within the range 0.01 to 0.09, which is consistent with our estimate here due to uncertainty in the region $A_{M2}$ and the choice of 20% for entrainment/surface flux ratio. We therefore use a constant value of $n_* = 0.066$ to parameterize the contribution of convection to $\hat{M}_{H_{bl}}$.

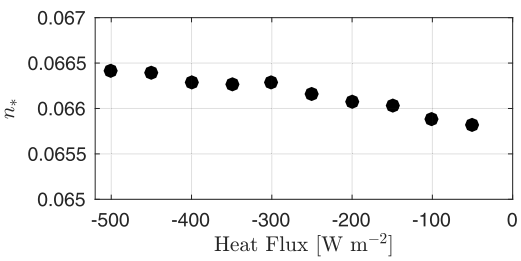


**Fig. 4.** Value of $n_*$ computed by Eq. (24) from column model simulations using the $k - \epsilon$-SG mixing in GOTM. Each point is the average value over the final five days of a ten day simulation.

### 3.2. $m_*$ for wind forced and rotating OSBL

The coefficient $m_*$ for mechanically-driven mixing includes the interaction of several physical mechanisms related to wind-driven mixing in one coefficient. It will vary depending on factors including surface currents, stratification, and surface waves. When surface wave effects and horizontal processes are neglected (as we have for this study), the mechanically driven turbulence is entirely due to instabilities associated with vertical shear in the Eulerian mean wind-driven current.

Previous studies (e.g. Gaspar, 1988) often employ a constant $m_*$ parameter. One study modifies this approach by introducing an exponential function with an e-folding depth set by the Ekman length (Oberhuber, 1993), which introduces mixing dependence on $u_*$, $|f|$, and $H_{bl}$. We will test these approaches by investigating $m_*$ diagnostically from one-dimensional simulations using the more complete $k-\epsilon$-SG parameterization.

In this section we investigate cases where the water column is initially stable and there is no destabilizing buoyancy force. In this case, Eq. (23) reduces to:

$$\hat{M}_{Hbl} = m_* u_*^3. \tag{28}$$

This equation is then used to compute $m_*$ from the $k-\epsilon$-SG simulations where $\hat{M}_{Hbl}$ is known. We then infer relations to parameterize $m_*$ to emulate $k-\epsilon$-SG without sensitivity to the time-step. In this section we only explore rotating simulations. We discuss non-rotating simulations in Section 3.5.

#### 3.2.1. No buoyancy forcing

We first investigate the scenario of a pure wind forced, rotating column using one-dimensional model simulations with $k-\epsilon$-SG. The model is simulated with four initial stratifications ($\partial\bar{\theta}/\partial z = [-0.04, -0.02, -0.01, -0.001]$ °C m$^{-1}$), three wind forcings ($\tau_x = [0.1, 0.5, 1]$ N m$^{-2}$), and four Coriolis frequencies (latitudes of [10, 30, 60, 90] °N) to investigate variability of $m_*$. The results are averaged over an inertial period to mitigate the effect of inertial oscillations. The values of $m_*$ for all simulations after 10 model days are shown in Fig. 5. The value of $m_*$ correlates with $H_{bl}|f|/u_*$, indicating reduced OSBL entrainment as $H_{bl}$ approaches the Ekman depth ($u_*/|f|$).

When the mean wind-input of mechanical energy to the currents is equal to the TKE-production, the mean-flow is in steady-state with the turbulence (darker shaded circles in Fig. 5). If the model is simulated until this criteria is reached, the $m_*$ values converge approximately to the red line function:

$$m_{*N} = c_{N1}(1 - [1 + c_{N2}\exp(-c_{N3}H_{bl}|f|/u_*)]^{-1}). \tag{29}$$

where $c_{N1} = .275$, $c_{N2} = 8$, and $c_{N3} = 5$. The robustness of this fit (29) to the model output was tested to $H_{bl}|f|/u_* = 0.1$, though significantly longer duration simulations are required to reach this criteria (not shown). When $H_{bl}|f|/u_*$ is less than about 0.3, the time required for the TKE production to equilibrate with the wind-input is often long (multiple inertial periods, which equals weeks at 10° latitude and months at 1° latitude). In this case, the balanced relation (red-line, 29) for $m_*$ is exceeded due to excitement of the currents beyond the Ekman balance, augmenting the shear production. It takes several inertial periods for this enhanced energy to be extracted from the mean shear and the inertial oscillations such that the shear-production balances the mean wind input. This effect is prominent when the inertial period is long (i.e. in lower latitudes), and it exists even if the wind speed is imposed gradually over an inertial period.

We might construct an alternate fit to the simulation data, which depends on the 10 day forcing time period of this experiment:

$$m_{*Nb} = c_{Nb1}\exp(-c_{Nb2}H_{bl}|f|/u_*), \tag{30}$$

where $c_{Nb1} = .5$ and $c_{Nb2} = 3$ in the blue line in Fig. 5. The fit of the data to this function is highly dependent on the duration of the simulation.

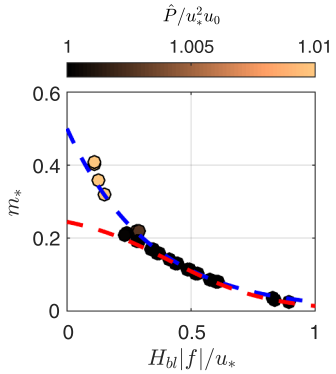


**Fig. 5.** Relation between $m_* = \hat{M}_{Hbl}/u_*^3$ and the non-dimensional boundary layer depth at four initial stratifications, three wind stress forcings, and four latitudes (ranging from 10 to 90° N). The dark colored circles represent integrated TKE production ($\hat{P}$) balanced with wind-input ($u_*^2u_0$, where $u_0$ is the surface current), while the lighter colors indicate the TKE production exceeds the wind-input. The blue line is an alternate exponential fit to the results and the red line is the fit to the fully balanced results only. (For interpretation of the references to colour in this figure legend, the reader is referred to the web version of this article.)

For a general application this approach is therefore not advisable. This result confirms that transience and hysteresis are important in determining $m_*$, particularly at lower latitudes.

#### 3.2.2. Stabilizing buoyancy forcing

We next investigate cases that include a stabilizing surface buoyancy flux. In this case we introduce an additional external parameter, $B_f$. We compute $m_*$ from the $k-\epsilon$-SG simulations for models with the identical four initial stratifications, three wind speeds and four latitudes as in the previous section. We also introduce four stabilizing heat fluxes ([25, 50, 75, 100] W m$^{-2}$). We first show the value of $m_*$ plotted against $H_{bl}|f|/u_*$ (Fig. 6, left panel). The scaling for $m_*$ is different from that found in the neutral case (Fig. 5).

The dashed red curve in Fig. 6 (left panel) is the curve found for the neutral $m_*$ (Eq. (29)). This curve is the lower limit of $m_*$ in this regime at a given $H_{bl}|f|/u_*$, suggesting the effect of the stabilizing heat flux is to increase $m_*$ from the neutral value (and supporting the $m_{*N}$ fit to $H_{bl}|f|/u_* = 0.15$). We subtract the value of $m_{*N}$ from the total $m_*$ and plot the residual $m_{*S} = m_* - m_{*N}$ against the non-dimensional relation $u_*^5|f|/B_f^2H_{bl}$. The non-dimensional relation $u_*^5|f|/B_f^2H_{bl}$ is the relevant non-dimensional parameter combination using scaling arguments from the shear-production (equivalent to the Obukhov length squared over the Ekman depth times the boundary layer depth). This relation correlates well with the model data and can therefore be used to

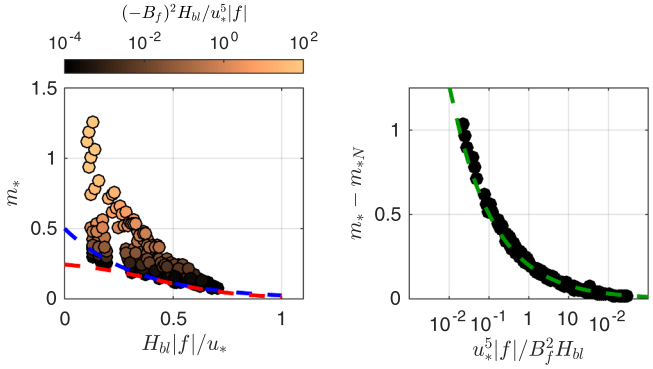


**Fig. 6.** (Left) Relation between $m_*$ and $H_{bl}|f|/u_*$ and (Right) relationship between $m_*$ and the non-dimensional relation $u_*^5|f|/B_f^2H_{bl}$ at a range of wind stress, latitudes, and stabilizing heat fluxes. Compare to the neutral case shown by Fig. 5.

parameterize $m_{*S}$ (Fig. 6, right panel). This indicates that the fractional potential energy change due to turbulence mixing increases either when the Obukhov length is reduced (more stratification to mix) or when the Ekman depth or boundary layer depth are increased (more energy available to mix).

In the stabilizing regime, the computed $m_*$ correlates well to the relationship:

$$m_{*S} = c_{S1}(B_f^2 H_{bl}/u_*^5|f|)^{c_{S2}}, \quad B_f < 0, \tag{31}$$

to parameterize $m_{*S}$ in the presence of a stabilizing surface flux and rotation (green dashed line in Fig. 6, where $c_{S1} = 0.2$ and $c_{S2} = 0.4$). This relationship (31) is applicable for a stabilizing surface buoyancy flux only (the destabilizing flux is discussed in Section 3.3), and $m_{*S} = 0$ otherwise. This fit is confirmed from simulations after roughly one inertial period spin-up from rest and tested with heat fluxes from 0 to 1000 W m$^{-2}$ at 1–90° latitude. This fit is never valid at $f = 0$, since the criteria for sustained forcing over multiple inertial cycles is not possible. Furthermore, forcing time-scales are not often equivalent to inertial time-scales at near-equatorial latitudes.

### 3.3. Coincident wind forcing with convection

We now consider the case with both wind-forced turbulence and convective turbulence. If we employ $n_* = 0.066$ and the $m_*$ relationship from neutral forcing (30) we over-estimate the total mixing in this scenario. One reason for over-estimating the mixing is straightforward. When the wind generates currents, the shear-instabilities generate TKE. A fraction of this TKE is dissipated and the remainder is available to mix stable stratification and create potential energy. When there is a destabilizing surface buoyancy flux, the mean stratification is unstable near the surface and therefore there is less stable stratification to mix.

The reduction of near-surface stable stratification in the presence of convection means the fraction of wind-driven TKE converted to potential energy may be reduced relative to the neutral case. The total TKE and total mixing increases relative to the individual (wind or convection alone) cases, but it is less than the sum of the individual processes. This simple explanation does not consider the interaction between shear-driven and convectively driven turbulent processes. It also ignores TKE flux away from the source region into the stable stratification below that mitigates this effect. However, this explanation may be used to approximate the effect of convection on mechanically driven mixing.

To demonstrate how significant the over-estimated mixing is, we compute $\hat{M}_{H_{bl}}$ over a range of both heating and cooling scenarios (-100 to 100 W m$^{-2}$) with a range of wind forcing and latitudes. We compare $\hat{M}_{H_{bl}}$ predicted using $n_*$ of 0.066 and $m_* = m_{*N} + m_{*S}$ from Eqs. (29) and (31) in Eq. (23) to that computed directly from the $k-\epsilon$-SG simulations. For the cases with destabilizing heat fluxes, the new formulation predicts more mixing than $k-\epsilon$-SG (Fig. 7, left). We confirm that the primary cause is the overestimated mechanical mixing by setting $n_* = 0$ in Eq. (23). In this case, we neglect the contribution of convection, but still predict a greater $\hat{M}_{H_{bl}}$ relative to $k-\epsilon$-SG (Fig. 7, right). This result shows that even when the mechanically driven dominates it can be significantly reduced due to convection.

### 3.4. Parameterizing the reduction of $m_*$ due to convection.

In this section we investigate the reduction of $m_*$ due to convection. We will examine the profile of the buoyancy flux after 10 days of simulation in both neutral and destabilizing wind-forced $k-\epsilon$-SG cases.

For a neutral case (Fig. 8, black line) we find a nearly linear profile in depth of the buoyancy flux to the mixing depth. The value $\hat{M}_{H_{bl}} = m_* u_*^3$ is the area under this region. If we approximate this area as triangular we can write $\hat{M}_{H_{bl}} = \frac{1}{2} W H_{bl}$ (where $W$ is width and $H_{bl}$ is height), in which case:

$$\hat{M}_{H_{bl}} = m_* u_*^3 = \frac{1}{2} H_{bl} W. \tag{32}$$

The value of $W$ here therefore equals $2m_* u_*^3/H_{bl}$.

For a case with a convective surface flux (Fig. 8, blue line) we find that a fraction of the OSBL has a positive (destabilizing) buoyancy flux. In the region with positive buoyancy flux the turbulence drives potential energy release due to gravitational instability. In this region no net TKE conversion to potential energy occurs. The vertical thickness of the region with negative $\overline{w'b'}$ is greatly reduced by the presence of surface cooling. We use this knowledge to approximate the reduction of $m_*$ proportionally to the fraction of the OSBL thickness with unstable stratification. We also note that the value of the buoyancy flux at the base of the OSBL is only slightly increased due to the addition of convection (e.g. width $W$). The increase in this width will depend on the ratio of mechanical forcing to buoyancy forcing of OSBL turbulence (or the ratio of the Obukhov depth and the boundary layer depth, $(u_*^3/\kappa B_f)/H_{bl}$).

We look at the effect of combined mechanical and buoyancy forcing more carefully in Fig. 9. The surface value of $\overline{w'b'}$ is (by definition) the negative of surface flux $B_f$. The value of $W$ is hypothesized to remain approximately $2m_* u_*^3/H_{bl}$ (ignoring additional contribution by the buoyancy flux to the entrainment flux). If we know $H_{bl}$, the area of $A$ in this diagram can be found without knowing $H_M$ or $H_G$. If the buoyancy is changing at a uniform rate in the boundary layer, $H_G/(-B_f)$ must equal $H_{bl}/([2m_* u_*^3/H_{bl}] - B_f)$, where $B_f$ is negative in convection. Using these relationships, the value of $H_G$ is written:

$$H_G = \frac{-B_f H_{bl}}{-B_f + 2m_* u_*^3/H_{bl}}. \tag{33}$$

From this expression we find the value of $H_M$:

$$H_M = H_{bl}\left(\frac{2m_* u_*^3/H_{bl}}{-B_f + 2m_* u_*^3/H_{bl}}\right). \tag{34}$$

Now, to get $A$ (or equivalently $\hat{M}_{H_{bl}}$) we multiply $1/2 \times H_M \times 2m_* u_*^3/H_{bl}$:

$$\hat{M}_{H_{bl}} = m_* u_*^3\left(\frac{2m_* u_*^3/H_{bl}}{-B_f + 2m_* u_*^3/H_{bl}}\right). \tag{35}$$

For this derivation we assumed that there was no additional downward flux of TKE to mitigate the effect we discuss here. One method to parameterize this reduction is to introduce a fractional, positive constant to the buoyancy flux in the denominator, $0 \le c_\psi \le 1$, which serves to represent the impact of interactions with dissipation, the ignored convective contribution to TKE increase, and other turbulent processes. Introducing this constant (which we estimate to be $\approx 0.67$ in the $k-\epsilon$-SG simulations), the quantity $\Psi = H_M/H_{bl}$ is written:

$$\Psi = \left(\frac{2m_* u_*^3}{c_\psi \max(0, -B_f)H_{bl} + 2m_* u_*^3}\right). \tag{36}$$

This correction is then multiplied by $m_*$ in the presence of a destabilizing surface buoyancy flux to approximate the reduction due to interaction of convective and wind-driven processes. In the simulations explored here, this effect is important during even relatively weak destabilizing surface buoyancy fluxes to correctly predict $\hat{M}_{H_{bl}}$.

We apply this correction to eliminate the over-estimation of $\hat{M}_{H_{bl}}$ (Fig. 10). The reduction of $m_*$ does not imply reduced total TKE relative to the isolated convection or wind forced case. It is fundamentally similar (but opposite) to the enhancement of $m_*$ found during a stabilizing buoyancy flux.

### 3.5. Non-rotating cases

In this section, we presented relations that are used to parameterize

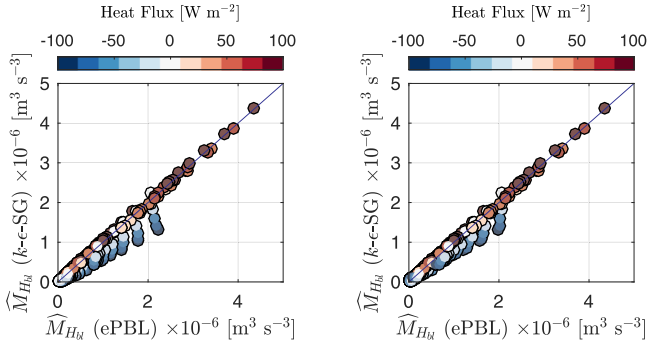


**Fig. 7.** (Y-axis) Total mixing computed from a column model with $k-\epsilon$-SG mixing vs (X-axis) total mixing predicted using (Left) the full ePBL parameterization with $m_*$ given by Eqs. (29) and (31) and (Right) the ePBL parameterization with the same $m_*$ but $n_*=0$. Results include four surface wind stress values, heat fluxes ranging from -100:100 W m$^{-2}$, and eight latitudes from 20 to 90° N. The blue line represents a 1:1 linear relationship. (For interpretation of the references to colour in this figure legend, the reader is referred to the web version of this article.)

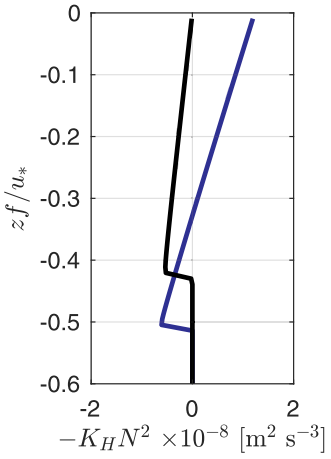


**Fig. 8.** Buoyancy flux profile with wind stress forcing of 0.1 N m$^{-2}$ for (black) no surface buoyancy flux and (blue) case with convective mixing forced by a -25 W m$^{-2}$ surface heat flux. (For interpretation of the references to colour in this figure legend, the reader is referred to the web version of this article.)

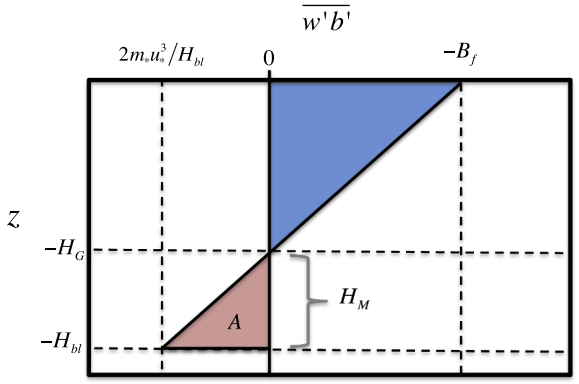


**Fig. 9.** Schematic for the derivation of the adjustment to the mixing, $\hat{M}_{H_{bl}}$, during convectively unstable buoyancy forcing. A linear buoyancy flux is given ranging from value $-B_f = w'b'_0$ at the surface to $2m_*u_*^3/H_{bl}$ at the boundary layer base. The depth where the buoyancy flux becomes stabilizing is denoted as $H_G$, such that $H_M = H_{bl} - H_G$ is the thickness of the regime where the buoyancy flux is associated with mixing.

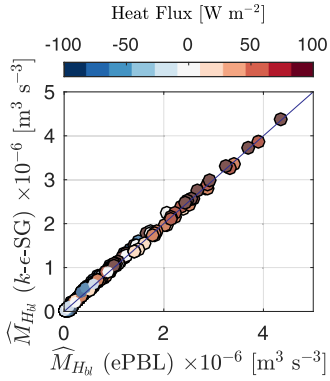


**Fig. 10.** (Y-axis) Total mixing computed from a column model with $k-\epsilon$-SG mixing vs (X-axis) total mixing predicted using the ePBL parameterization with $m_*$ given by Eqs. (29), (31) and (36) and $n_*=0.066$. Results include four surface wind stress values, heat fluxes ranging from -100-100 W m$^{-2}$, and eight latitudes from 20 to 90° N. Similar to Fig. 7, but here correction $\Psi$ is applied in ePBL.

variability in $m_*$ for cases with $|f| > 0$. We did not explore in detail the value of $m_*$ when $f=0$. The behavior of the $m_*$ coefficient is quite different between these two regimes.

At the equator, skillful parameterization for $m_*$ (not-shown) correlates with $HN_0/u_*$, where $N_0$ is the characteristic buoyancy frequency of the entrained water (following Pollard et al., 1972). We deliberately do not investigate details of this scaling since there is no obvious transition between $N_0$ based scaling and $|f|$ based scaling. In the following section we present a method to infer mixing coefficient profiles from the WMBL method and the $n_*$ and $m_*$ values estimated in this section.

## 4. A framework to predict turbulent mixing in climate simulations

For climate simulations we propose that a useful parameterization is one that consistently simulates the energetics of turbulent mixing independent of time-step and resolution. We use the results of the previous sections to construct a vertical profile of the mixing coefficient that provides a numerically insensitive mixing parameterization. The full mixing parameterizations will include contributions to the total OSBL mixing coefficient from a new OSBL parameterization (hereafter the energetic Planetary Boundary Layer, or ePBL) with the resolved shear-driven mixing parameterization of JHL. We define the vertical profile of the vertical turbulent mixing coefficient for use in an ocean climate model as:

$$K(z) = F_x(K_{ePBL}(z), K_{JHL}(z), K_n(z)), \tag{37}$$

where $F_x$ is a yet-to-be-determined functional form, $K_{ePBL}$ is a mixing coefficient motivated by WMBLs introduced in this section, $K_{JHL}$ is the resolved-shear driven mixing coefficient of JHL, and $K_n$ represents mixing from arbitrary other sources.

The implementation of the JHL parameterization is not employed for convective conditions and is sensitive to resolution and time-step when $|f| > 0$ (see Section 2). The $K_{ePBL}$ component of the parameterization therefore deliberately targets these two tasks for a climate model. The $K_{ePBL}$ component is a boundary layer mixing parameterization and is only intended to predict mixing in the OSBL driven by the surface fluxes. Therefore, the $K_{JHL}$ component and $K_n$ component are always required for turbulent mixing due to processes including internal shear driven mixing (JHL) and internal wave breaking. We express the total mixing coefficient using an undefined function in Eq. (37) to emphasize that it is not generally sufficient to use a linear combination of mixing coefficients from separate energy sources when they occur together (e.g. as shown in Section 3.3 for convective and mechanical turbulence).

### 4.1. The ePBL mixing coefficient

The ePBL mixing coefficient is inspired by the WMBL approach and its insensitivity to long time-steps and coarse vertical resolution. Here we will relax the assumption in WMBLs of vertical homogeneity within the OSBL (motivated by Hallberg, 2003). The critical component of ePBL is that the mixing coefficient and the depth of the boundary layer are explicitly constrained to satisfy the potential energy change due to turbulent mixing imposed using Eq. (23).

We define the ePBL mixing coefficient using the general form of:

$$K_{ePBL}(z) = C_K w_t l, \tag{38}$$

where $w_t$ is a turbulent velocity scale and $C_K$ is a coefficient. In KPP, a non-gradient mixing contribution is included to more accurately parameterize convection (see Large et al., 1994). We neglect this component here as it does not significantly affect our results and its accurate parameterization in the ocean remains a topic of research (e.g. Van Roekel et al., 2018). ePBL is designed to constrain the total potential energy change due to turbulent mixing and solve implicitly for the impacts of mixing on the density and velocity profiles without sensitivity to vertical resolution and time-step. The primary purpose of Section 3 is to establish methods for parameterizing $m_*$ and $n_*$ to serve as the energetic constraint for vertical mixing in climate simulations. In this subsection we present a method to estimate the vertical profile of the turbulent mixing coefficients, $K_{ePBL}$. The exact value of the mixing coefficient and therefore the values of $w_t$ and $l$ in Eq. (38) are not critical for maintaining the integrated potential energy change constraint. However, the vertical profile of the mixing coefficient is important as it determines the vertical profile of the mean current and scalars near the surface.

### 4.2. Defining the turbulent length scale

We begin by assuming the mixing length follows wall theory near the surface ($l \to |z|$). This approach is simplistic in the real ocean due to the presence of wave breaking and Langmuir turbulence (e.g Craig and Banner, 1994; Sullivan et al., 2007). The wave effects can be parameterized using a minimum "roughness length" $z_0$. If law-of-the-wall is also a reasonable approximation for the mixing length at the lower boundary of the OSBL, we can use a length scale equation of:

$$l = (z_0 + |z|)\frac{(H_{bl} - |z|)}{H_{bl}}. \tag{39}$$

This profile is expressed in a general way as:

$$l = (z_0 + |z|)\left(\frac{H_{bl} - |z|}{H_{bl}}\right)^{\gamma}, \tag{40}$$

where $\gamma$ is the coefficient that determines the profile. Setting $\gamma = 2$ gives a mixing length profile similar to that of KPP (Large et al., 1994). $k-\epsilon$-SG simulations simulations indicate that the value of $\gamma$ is variable, depending on factors such as latitude and buoyancy flux. These details introduce only small errors in the context of this study and therefore are not investigated.

The mixing-length does not typically become zero at the bottom of the OSBL, which may be either the ocean interior or the ocean bottom. We therefore introduce a bottom length scale $l_b$, which can depend on bottom roughness or local stratification:

$$l = (z_0 + |z|) \times \max\left[\frac{l_b}{H_{bl}}, \left(\frac{H_{bl} - |z|}{H_{bl}}\right)^{\gamma}\right]. \tag{41}$$

Alternative approaches (e.g. Gaspar et al., 1990) may also be employed to estimate the length scale. We choose the form (41) since it is simple to implement in an ocean model and our results are consistent with the $k-\epsilon$-SG approach (see Section 5).

### 4.3. Defining the turbulent velocity scale

We do not predict the TKE prognostically and therefore approximate the vertical TKE profile to estimate $w_t$. An estimate for the mechanical contribution to the velocity scale follows the standard two-equation approach. In one and two-equation second-order $K$ parameterizations the boundary condition for the TKE is typically employed as a flux boundary condition:

$$K\frac{\partial k}{\partial z}\bigg|_{z=0} = c_\mu^0 u_*^3. \tag{42}$$

The profile of $k$ decays in the vertical from $k \propto (c_\mu^0)^{2/3}u_*^2$ toward the base of the OSBL. Here we assume a similar relationship to estimate the mechanical contribution to the TKE profile. The value of $w_t$ due to mechanical sources, $v_*$, is estimated as $v_*(z=0) \propto (c_\mu^0)^{1/3}u_*$ at the surface. Since we only parameterize OSBL turbulent mixing due to surface forcing, the value of the velocity scale is assumed to decay moving away from the surface. For simplicity we employ a linear decay in depth:

$$v_*(z) = (c_\mu^0)^{1/3}u_*\left(1 - a\cdot\min\left[1, \frac{|z|}{H_{bl}}\right]\right), \tag{43}$$

where $1 > a > 0$ has the effect of making $v_*(z = H_{bl}) > 0$. Making the constant coefficient $a$ close to one has the effect of reducing the mixing-rate near the base of the boundary layer, thus producing a more diffuse entrainment region. Making $a$ close to zero has the effect of increasing the mixing at the base of the boundary layer, producing a more 'step-like' entrainment region.

An estimate for the buoyancy contribution is found utilizing the convective velocity scale:

$$w_*(z) = C_{w_*}\left(\int_z^0 \overline{w'b'}dz\right)^{1/3}, \tag{44}$$

where $C_{w_*}$ is a non-dimensional empirical coefficient. Convection in one and two-equation closure causes a TKE profile that peaks below the surface. The quantity $\overline{w'b'}$ is solved for in ePBL as $KN^2$.

These choices for the convective and mechanical components of the velocity scale in the OSBL are then added together to get an estimate for the total turbulent velocity scale:

$$w_t(z) = w_*(z) + v_*(z). \tag{45}$$

This approach to diagnose a turbulent velocity scale is highly empirical and is therefore not expected to satisfy all general properties of turbulence theory. In reality, the two effects are not linearly summed, however, this approximation is reasonable to estimate of the velocity scale for this purpose. The value of $a$ in Eq. (43) is arbitrarily chosen to be 0.95 here. We explored the use of alternative velocity scales (such as KPP, which extends similarity theory through the boundary layer) and find little sensitivity over a wide range of realistic conditions. Future research efforts will investigate methods to improved the estimate of $w_t$ (such as the effect of surface waves).

### 4.4. Summarizing the ePBL implementation

We now review the findings of this section and summarize the ePBL framework we implement in our model. The ePBL mixing coefficient (38) is found by multiplying a velocity scale (Eq. (45)) by a length scale (Eq. (41)). The precise value of the coefficient $c_K$ in Eq. (38) does not significantly alter the prescribed potential energy change constraint. A reasonable value is $c_K \approx 0.55$ to be consistent with other approaches (e.g. Umlauf et al., 2005).

The boundary layer thickness ($H_{bl}$) within ePBL is based on the depth where the energy requirement for turbulent mixing of density exceeds the available energy following Eq. (23). $H_{bl}$ is determined by the energetic constraint imposed using the values of $n_*$ and $m_*$. An

iterative solver is required because $m_*$ and the mixing length are dependent on $H_{bl}$.

We use a constant value for convectively driven TKE of $n_* = 0.066$. The parameterizations for $m_*$ are formulated specifically for the regimes where $K_{JHL}$ is sensitive to model numerics ($|f|\Delta t \approx 1$). We find a neutral value for $m_*$ given by Eq. (29), which is augmented under surface heating by Eq. (31) and reduced under convection by Eq. (36).

### 4.5. Combining the ePBL and JHL mixing coefficients

We now address the combination of the ePBL mixing coefficient and the JHL mixing coefficient. The function $F_x$ in Eq. (37) cannot be the linear sum of $K_{ePBL}$ and $K_{JHL}$. One-reason this sum is not valid is because the JHL mixing coefficient is determined by resolved current shear, including that driven by the surface wind. The wind-driven current is also included in the ePBL mixing coefficient formulation. An alternative approach is therefore needed to avoid double counting.

$K_{ePBL}$ is not used at the equator here as scalings are only investigated when $|f| > 0$. The solution we employ is to use the maximum mixing coefficient of the two contributions,

$$K(z) = \max(K_{ePBL}(z), K_{JHL}(z)), \tag{46}$$

where $m_*$ (and hence $K_{ePBL}$) is constrained to be small as $|f| \to 0$. This form uses the JHL mixing coefficient when the ePBL coefficient is small.

Eq. (46)is a reasonable approach when the wind-driven mixing dominates, since both JHL and ePBL give a similar solution when deployed optimally. One weakness of this approach is the tropical region, where the shear-driven ePBL $m_*$ coefficient is not formulated. The JHL parameterization is skillful to simulate this mixing, but does not include the contribution of convection. The convective portion of $K_{ePBL}$ should be combined with $K_{JHL}$ in the equatorial region when shear and convection occur together (though they are not linearly summed, see Fig. 7). In this study we always employ the maximum value (46), since the mixing coefficient is consistent with the $k-\epsilon$-SG approach despite this limitation (Section 5). Future research will investigate more complete integration of the $K_{ePBL}$ and $K_{JHL}$ energetics.

## 5. Evaluation of ePBL against $k-\epsilon$

We now evaluate ePBL through comparison with a model using the $k-\epsilon$-SG parameterization. The $k-\epsilon$-SG simulations are used to find $m_*$ and $n_*$ and determine the coefficients for ePBL. Therefore, intercomparison of free running simulations utilizing both $k-\epsilon$-SG and ePBL is a logical metric for evaluating ePBL's capability to reproduce the $k-\epsilon$-SG energetic constraint and test sensitivity to time-step and vertical resolution.

The ePBL parameterization is included in a one-dimensional version of the MOM6 ocean model (Adcroft et al., 2018). Here, we show results where the MOM6 model has been simulated with two set-ups. First, we employ a 1 m constant vertical grid spacing and 1200 s time-step. The second set-up tests coarse resolution used for climate models and employs a 10 m vertical grid spacing and a 7200 s time-step. The $k-\epsilon$ experiments are run with a 1 m vertical grid spacing and a 10 s time-step, which ensures that the evolution of the turbulent quantities with the mean ocean-state are accurately captured (Fig. 2). For all simulations here the column is initialized with a constant, stable stratification of 0.01 °C m$^{-1}$.

We begin with a broad model inter-comparison, and then focus on several case-studies. For the broad comparison, we vary the surface heat flux from -100 to 100 W m$^{-2}$ in increments of 25 W m$^{-2}$ to encompass a range from stabilizing to convecting. We choose a moderate wind stress for this demonstration of 0.2 N m$^{-2}$ ($U_{10} \approx 10$ m s$^{-1}$), which allows for a range of relative strengths of mechanical and buoyancy forced turbulence to be tested. This range of conditions is limited to relatively deep Obukhov depths $|L_O| > 25$ ($L_O = u_*^3/\kappa B_f$) in both stabilizing or destabilizing regimes. In strongly destabilizing regimes the value of $n_*$ for this parameterization is well-constrained and the effect of mechanical mixing is minimal. Strongly stabilizing regimes in the realistic ocean (Heat fluxes $\approx$ 500 W/m$^2$ and wind speeds $<$ 5 m/s) are resistant to turbulent mixing below just a few meters and therefore are not included in this comparison. We simulate the set-up for latitudes ranging from the equator to 90° in 10° increments. The average temperature over the top 10 m after 10 simulation days is compared from all 90 simulations to evaluate model performance.

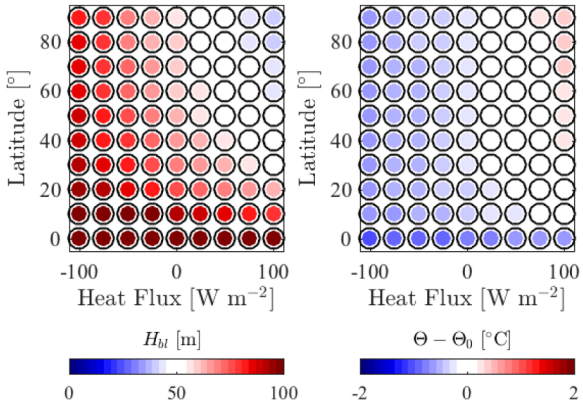


**Fig. 11.** Result after 10 days for 90 simulations using $k-\epsilon$-SG where the color of each circle represents (Left) $H_{bl}$ estimated from $k-\epsilon$-SG and (Right) change in temperature from the initial temperature of the upper 10 m of the water column. In each panel the corresponding latitude and surface heat flux for each simulation (negative being destabilizing) are distinguished by the position of the circle on $y$ and $x$ axis, respectively. The cases are all forced with a steady wind stress of 0.2 N m$^{-2}$. The OSBL depth is diagnosed for $k-\epsilon$-SG based on where the mixing length is less than 0.1 m.

We first show the resulting temperature change and the final OSBL depth after 10 simulation days using the $k-\epsilon$-SG model for all 90 simulations (Fig. 11). There is significant variability in the OSBL depth (left panel) over the simulations, where rotation, wind forcing, and buoyancy fluxes all contribute in various regimes. The temperature change (right panel) ranges from surface cooling of up to about 1 °C to surface warming of a fraction of 1 °C.

We simulate MOM6 experiments with (i) JHL only (no $K_{ePBL}$), (ii) ePBL only (no $K_{JHL}$), and (iii) with the full set-up employing the maximum turbulent mixing coefficient predicted from ePBL and JHL (Eq. (46)). In the second and third case, the convective turbulence is parameterized with a value of $n_* = 0.066$. JHL is meant to parameterize mixing due to shear-instability only.

### 5.1. Broad comparison, $k-\epsilon$ vs JHL, ePBL, and JHL + ePBL

We begin with a comparison using ePBL and JHL at identical 1 m grid spacing to the $k-\epsilon$ model. The energetic constraints in ePBL are not sensitive to the grid thickness, but the simulation of cooling and heating in the model is. Therefore, we first compare the similar model set-up. In these simulations, the model with JHL performs well relative to the $k-\epsilon$-SG simulations in the lower latitudes (Fig. 12, upper-left panel). The JHL scheme does not perform well away from the equator, particularly in the presence of surface heating. One reason is that JHL performance is limited by the longer time-step (JHL w/ 1200 s and $k-\epsilon$-SG with 10 s).

When the model is simulated with ePBL alone we find the opposite result to using JHL (Fig. 12, upper-center panel). The ePBL scheme performs well away from the equator, but has not been designed for the regime where $|f|$ becomes small. The surface temperature differences with ePBL + JHL are small relative to $k-\epsilon$-SG for all cases simulated. This result shows that the two parameterizations work in tandem to produce a good result (Fig. 12, upper-right panel).

We next show the simulations using a 10 m grid spacing and 7200 s

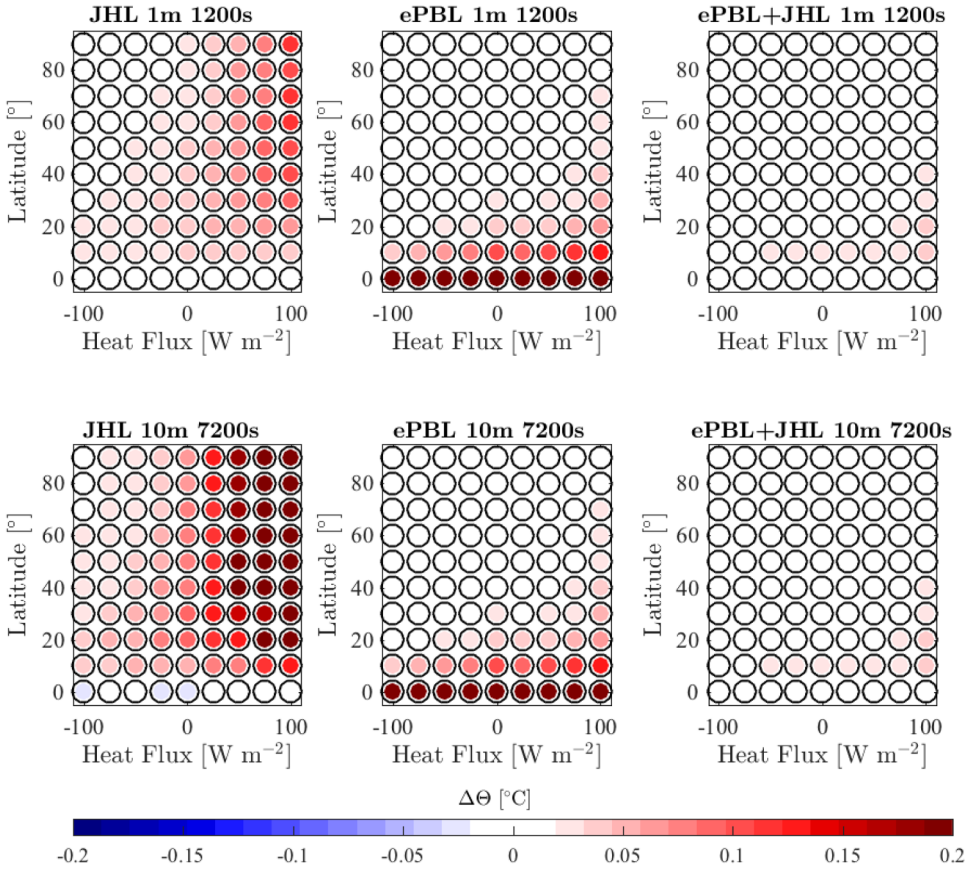


**Fig. 12.** Difference between top 10 m average temperature (°C) with 1 m grid spacing in $k-\epsilon$-SG simulation and (upper panels) 1 m grid spacing with 1200 s time-steps in MOM6 for (Left) JHL shear-driven mixing, (center) with ePBL mixing, and (right) with the maximum mixing coefficient from ePBL and JHL used and (lower panels) 10 m grid spacing with 7200 s time-steps in MOM6. In each panel the corresponding model latitude and surface heat flux (negative being destabilizing) are given by the $y$ and $x$ axis, respectively. The cases are all forced with a wind stress of 0.2 N m$^{-2}$.

time-step in MOM6 (Fig. 12, bottom panels). In this case the performance of JHL away from the equator is degraded (left panels). The ePBL performance remains consistent with the previous experiment (center panels). The ePBL + JHL result remains reasonable compared to $k-\epsilon$-SG, showing that this framework is reasonable even at the coarse vertical grids and long time-steps of ocean climate models.

### 5.2. Case study 1, convection

We now present vertical profiles of the quantities simulated by the column models to demonstrate select results for the full column. First we show a case with a surface wind stress of 0.2 N m$^{-2}$ and surface buoyancy flux of -100 W m$^{-2}$ (cooling) located at 40° N (Fig. 13). For each scheme in MOM6 (ePBL, JHL, ePBL + JHL) we present the results using a 1200 s time-step and 1 m vertical grid spacing (dashed lines). For the combined JHL + ePBL approach we also include a 7200 s time-step and 10 m vertical grid spacing (x's). The JHL scheme is clearly inadequate for this case because it neglects convectively driven TKE. In this case ePBL closely matches the mixing predicted by $k-\epsilon$-SG. The mixing coefficients near the base of the OSBL are different, which is primarily due to the $k-\epsilon$-SG stability functions. In $k-\epsilon$-SG the turbulent diffusivity is computed from the turbulent viscosity through a Prandtl number as a function of the Richardson number. In the other simulations the Prandtl number is assumed one for simplicity. The temperature and current profiles are not very sensitive to this difference, showing the parameterization works as intended despite this simplification.

### 5.3. Case study 2, equatorial wind-driven

Next, we investigate the neutral (no buoyancy force) case with a wind stress of 0.2 N m$^{-2}$ at the equator (Fig. 14). The ePBL parameterization by itself is inadequate at this location because the Coriolis frequency tends towards zero and no parameterization has been provided for this regime. The model with the ePBL parameterization only (blue) therefore performs poorly. The model with ePBL and JHL (green) agrees with the JHL only model (red), showing that JHL sufficiently controls the mixing via (46). The JHL experiment performs well relative to $k-\epsilon$-SG and shows little sensitivity to the tested time-step differences.

### 5.4. Case study 3, mid-latitude wind-driven, stabilizing buoyancy flux

Finally, we show the simulation with a warming surface (sensible) heat flux of 100 W m$^{-2}$ and a 0.2 N m$^{-2}$ wind stress located at 40° N (Fig. 15). Here we find that the model with the JHL scheme alone is unable to predict the proper mixing coefficient due to the long time-step. We find that using ePBL alone in the model compares closer to the $k-\epsilon$ result. Using ePBL in tandem with JHL is not significantly different from ePBL alone, supporting the maximum value approach of (46). The shape of the mixing coefficient is similar between the ePBL formulations and $k-\epsilon$-SG.

## 6. Discussion

We introduce a framework for the OSBL that emphasizes constraining the potential energy change by turbulent mixing for climate

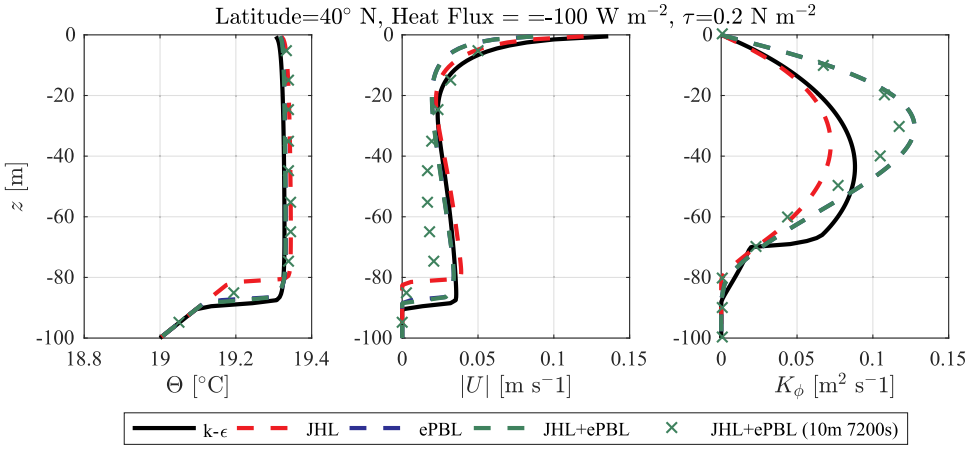


**Fig. 13.** (Left) Temperature, (Center) current magnitude, and (Right) turbulent mixing coefficient for 1D column simulations of the OSBL after 10 days. Latitude, wind stress, and heat flux are given by the panel titles. The green and blue lines are nearly identical (and therefore difficult to distinguish) in each panel. $k-\epsilon$ simulations use a time-step of 10 s, schemes given by dashed lines use a time-step of 1200 s, and the x's use a time-step of 7200 s. (For interpretation of the references to colour in this figure legend, the reader is referred to the web version of this article.)

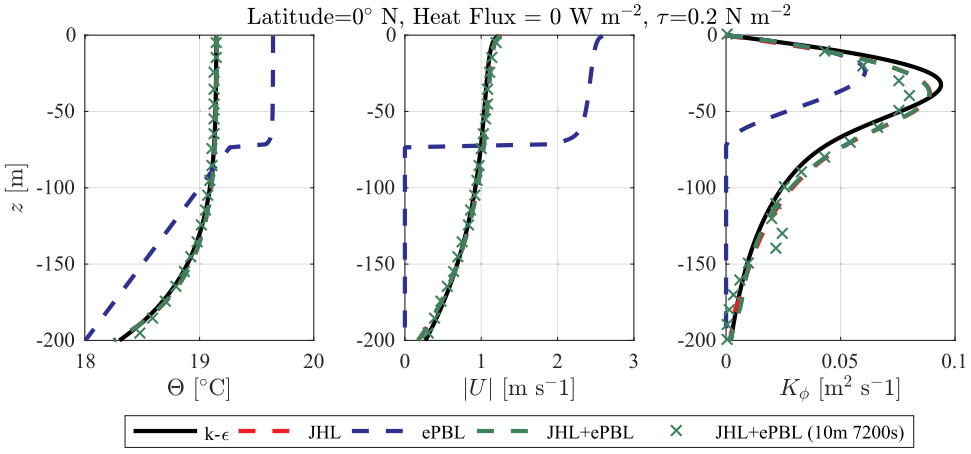


**Fig. 14.** (Left) Temperature, (Center) current magnitude, and (Right) turbulent mixing coefficient for one-dimensional simulations of the OSBL after 10 days. Latitude, wind stress, and heat flux are given by the panel titles. $k-\epsilon$ simulations use a time-step of 10 s, schemes given by dashed lines use a time-step of 1200 s, and the x's use a time-step of 7200 s. The black, red, and green lines are nearly identical in all three panels. (For interpretation of the references to colour in this figure legend, the reader is referred to the web version of this article.)

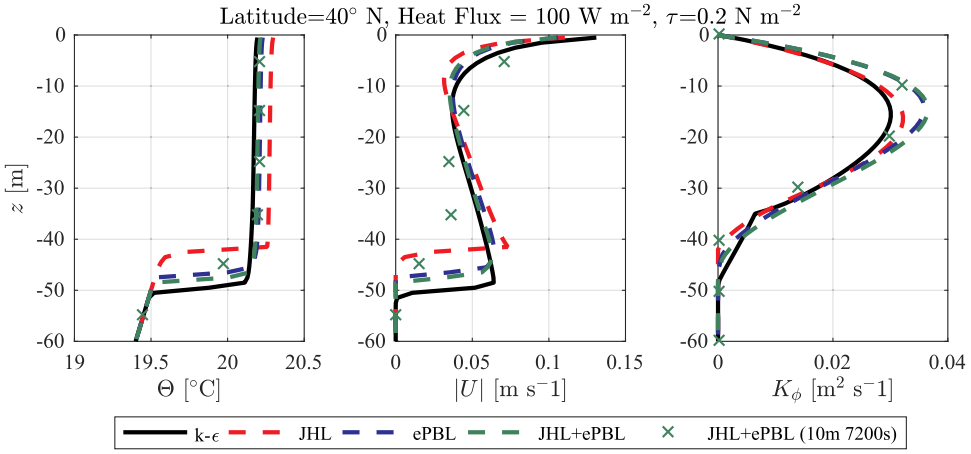


**Fig. 15.** (Left) Temperature, (Center) current magnitude, and (Right) turbulent mixing coefficient for one-dimensional simulations of the OSBL after 10 days. Latitude, wind stress, and heat flux are given by the panel titles. $k-\epsilon$ simulations use a time-step of 10 s, schemes given by dashed lines use a time-step of 1200 s, and the x's use a time-step of 7200 s. The green and the blue lines are nearly identical. (For interpretation of the references to colour in this figure legend, the reader is referred to the web version of this article.)

model applications. The ePBL component exploits relationships between this mixing constraint and external parameters. We also employ an existing parameterization (JHL) that resolves shear-driven mixing with limited sensitivity to model time-step when the Coriolis parameter is small. The ePBL method mitigates model sensitivity to time-step and vertical resolution. ePBL therefore can supplement prognostic TKE-based parameterizations like JHL or $k-\epsilon$ in climate simulations.

The new parameterization is demonstrated to simulate energetically consistent boundary layer mixing with time-steps as long as 7200 s and grid spacing as coarse as 10 m. We have not addressed several aspects that are relevant for general OSBL modeling. For example, we deliberately exclude horizontal property gradients in this study. Processes related to horizontal gradients (ocean fronts) are important in the OSBL, and alternative schemes are required to include these effects in ocean models (e.g. Fox-Kemper et al., 2011; Bachman et al., 2017). We review additional considerations that require investigation to improve model performance in this section.

### 6.1. Effects of surface waves in ePBL

Wave breaking (see Craig and Banner, 1994; Melville, 1996; Terray et al., 1996) and Langmuir turbulence (see Craik and Leibovich, 1976; Skyllingstad and Denbo, 1995; McWilliams et al., 1997; Belcher et al., 2012; D'Asaro et al., 2014) are important components of upper ocean turbulence and mixing. Breaking surface waves inject turbulent energy at the ocean surface, with vertical dissipation scaling with the wave height (see Craig and Banner, 1994; Terray et al., 1996; Melville, 1996). Langmuir turbulence, which is due to interaction of wave-driven Stokes drift with background turbulence, impacts OSBL dynamics through counter-rotating vortices with spatial-scales of the OSBL thickness. These structures lead to enhanced vertical velocities and entrainment (Skyllingstad and Denbo, 1995; McWilliams et al., 1997). Modifications to include Langmuir turbulence in second-order closure (Kantha and Clayson, 2004; Harcourt, 2013; 2015) and KPP (Reichl et al., 2016; Li et al., 2016) emphasize its importance for OSBL parameterization on both weather and climate scales. It is hypothesized that turbulence due to Langmuir circulations interacts with turbulence due to wave breaking, further enhancing mixing and entrainment (Noh et al., 2004; Sullivan et al., 2007; McWilliams et al., 2012).

Recent studies demonstrate that wave-enhanced OSBL parameterizations improve ocean climate simulations, particularly in high latitudes (Fan and Griffies, 2014; Li et al., 2016). The ePBL framework will require modification to include the contribution of waves to OSBL mixing for realistic climate implementation. This can be done by introducing an additional Stokes production term with properly calibrated dissipation in Eq. 23. This modification results in an additional $m_*$ source related to the Langmuir number (the non-dimensional relationship between Stokes and Shear production). For brevity, we reserve presentation of the surface wave effect within this framework for a separate study.

### 6.2. Transient forcing in ePBL

In tropical regions we found significant transient variability in $m_*$ due to the long inertial period. In extra tropical regions transient processes can produce inertial resonance, contributing to enhanced turbulent entrainment (see Skyllingstad et al., 2000). Predicting $m_*$ for this scenario would require a flow-dependent parameter to be considered, possibly using the wind energy input term. This process could be incorporated within the ePBL framework to improve performance for mesoscale ocean dynamics and finer submesoscale fronts and filaments. The transient forcing scenario will require attention if this scheme is utilized in models with fine horizontal resolution ( $< 10$ km). The effect of the diurnal cycle is also important in near-surface mixing and may require further modification to the ePBL approach, although it is currently in use in a coupled climate model with a diurnal cycle and provides reasonable performance (Adcroft et al., in prep). The transient events may average out in long simulations, but due to hysteresis effects such as ocean heat uptake under storms (e.g. Bueti et al., 2014) this scenario requires careful consideration for climate models at high (storm-resolving) resolutions. It is possible that the effects of transient forcing are too complex for the simple ePBL framework. In this case, alternative methods to mitigate time-step sensitivity to vertical mixing will be required. One possibility is to introduce convection to JHL and to investigate methods to mitigate degraded performance in the presence of rotation.

### 6.3. Length and velocity scales in ePBL

The ePBL mixing length scale is estimated from the distance between the surface and the OSBL depth. The velocity scale is estimated based on the buoyancy production and surface wind stress. In the test scenarios explored here this approach provides reasonable vertical distribution of the mixing coefficients. In the ocean, the mixing length and velocity scale are dependent on characteristics of the turbulence including whether it is mechanically driven or buoyancy driven (Moeng and Sullivan, 1994) and the effect of surface waves (Craig and Banner, 1994; Reichl et al., 2016). The length-scale and the velocity scale and the sensitivity of the resultant model to the mixing coefficients need to be explored further in realistic climate simulations.

## 7. Conclusion

The energetic Planetary Boundary Layer (ePBL) framework is designed to provide the vertical mixing coefficient used to simulate the impact of ocean surface boundary layer (OSBL) turbulence in ocean climate simulations. Computational restrictions in climate models dictate vertical resolution and time-steps that are sub-optimal for use of prognostic TKE turbulence closure methods (see Fig. 2). The time-step sensitivity of TKE closure is most notable in extra-tropical regions, where there is coupling between turbulence evolution and rotational effects on the mean state. We develop an alternative parameterization for this regime, which is combined with an equilibrium resolved shear parameterization (Jackson et al., 2008) to provide global estimates of OSBL mixing coefficients with little sensitivity to vertical resolution and time-step.

The vertical profile of the mixing coefficient satisfies mixing constraints based on the increase in potential energy due to turbulent mixing. Two turbulent generation processes are included here: shear production and buoyant production. Contributions due to other processes, including surface waves, are not included though are not precluded as an extension of this work.

The shear-production is included by parameterizing the energy available for mixing from the OSBL thickness, the surface friction velocity, the Coriolis frequency, and the surface buoyancy flux. We have demonstrated that these factors provide an accurate parameterization (for parameter $m_*$) of the energy available for mixing in extra-tropical regions (see Section 4.4). The convective contribution to the TKE budget is estimated based on previous observational results and simulations using $k-\epsilon$-SG. We find that the $n_*$ parameter (the fraction of convectively released TKE converted to potential energy) is approximately constant with a value of 0.066. These values of $m_*$ and $n_*$ are used to determine the turbulent mixing coefficients and combined with the resolved-shear JHL mixing coefficients. The present state-of-the-science NOAA Geophysical Fluid Dynamics Laboratory ocean climate model is being developed to utilize this scheme and future studies will demonstrate its performance within a coupled climate model.

## Acknowledgements

We thank Dr Stephen Griffies and Dr Alistair Adcroft for insightful discussion pertaining to the development of this manuscript. We also

thank Dr Stephen Griffies and Dr Sonya Legg for comments on drafts of this manuscript. We thank three anonymous reviewers for their constructive comments and helping to clarify the scope and presentation of this paper. BR is supported at NOAA/GFDL through the Cooperative Institute for Climate Science at Princeton University and the Princeton Environmental Institute at Princeton University through the Carbon Mitigation Initiative.

## Appendix A. Symbols and Acronyms

A comprehensive list of symbols used multiple times within the text and their mks units is given by tables A.1 and A.2. Acronyms used within the text are defined in Table A.3.

**Table A1**
Symbols.

| Variable | Definition |
|---|---|
| $\alpha$ | Thermal expansion coefficient [$^\circ$ C$^{-1}$] |
| $\alpha^*$ | JHL $F^*$ coefficient |
| $b$ | Buoyancy [m s$^{-2}$] |
| $B_f$ | Surface buoyancy flux [m s$^{-2}$] (positive into ocean) |
| $C_N$ | JHL Dissipation coefficient, buoyancy |
| $C_M$ | JHL Dissipation coefficient, shear |
| $c_{1\epsilon}$, $c_{2\epsilon}$, $c_{3\epsilon}$ | $k-\epsilon$ dissipation coefficients |
| $c'_\mu$ | Stability function for scalar |
| $c_\mu$ | Stability function for momentum |
| $c^0_\mu$ | Surface TKE condition in two-equation closures |
| $c_\psi$ | Constant in ePBL $\Psi$ factor |
| $C_K$ | Coefficient in ePBL $K_\phi$ equation |
| $C_{w_*}$ | Coefficient in ePBL $v_*$ |
| $\epsilon$ | Total turbulent dissipation [m$^2$ s$^{-3}$] |
| $f$ | Coriolis parameter [s$^{-1}$] |
| $F^*$ | JHL $K$ equation source |
| $g$ | Gravitational acceleration [m s$^{-2}$] |
| $H_{bl}$ | Boundary layer thickness [m] |
| $H_G$ | Convective production layer thickness [m] |
| $H_M$ | Entrainment layer thickness [m] |
| $k$ | TKE [m$^2$ s$^{-2}$] |
| $\kappa$ | von Kárman constant [ $\approx 0.4$] |
| $K_M$ | Turbulent viscosity [m$^2$ s$^{-1}$] |
| $K_\phi$ | Turbulent diffusivity [m$^2$ s$^{-1}$] |
| $l$ | Turbulent master length scale [m] |
| $m_*$ | Mechanical TKE flux coefficient |
| $m_2$ | Surface TKE flux coefficient |
| $m_3$ | Shear-driven TKE flux coefficient |
| $m_d$ | Dissipative TKE flux coefficient |
| $\hat{M}_{H_{bl}}$ | Integrated TKE mixing rate [m$^3$ s$^{-3}$] |
| $n_*$ | Buoyant TKE flux coefficient |
| $N$ | Buoyancy frequency [s$^{-1}$] |

**Table A2**
Symbols (cont.).

| Variable (cont.) | Definition |
|---|---|
| $\nu_\phi$ | Molecular diffusivity [m$^2$ s$^{-1}$] |
| $\omega$ | Turbulent time scale [s$^{-1}$] |
| $\Psi$ | ePBL factor for shear and buoyant forced TKE |
| $Ri_g$ | Gradient Richardson number |
| $\rho$ | Density [kg m$^{-3}$] |
| $S$ | Shear frequency [s$^{-1}$] |
| $\sigma_k$ | Turbulent Schmidt number for TKE |
| $\tau$ | Wind stress [N m$^{-2}$] |
| $\theta$ | Potential temperature [$^\circ$ C] |
| $u_i$ | Horizontal wind/current [m s$^{-1}$] |
| $u_*$ | Water friction velocity [m s$^{-1}$] |
| $w$ | Vertical current [m s$^{-1}$] |
| $w'b'$ | Buoyancy flux [m$^2$ s$^{-3}$] (positive stabilizing) |
| $w_e$ | Entrainment velocity [m s$^{-1}$] |
| $w_t$ | Turbulent velocity scale [m s$^{-1}$] |
| $x_i$ | Horizontal position [m] |
| $z$ | Vertical position [m] |

**Table A3**
Acronyms.

| Acronym | Definition |
|---|---|
| GOTM | General Ocean Turbulence Model |
| JHL | Jackson et al. (2008) Parameterization |
| KPP | K-Profile Parameterization |
| MOM | Modular Ocean Model |
| OSBL | Ocean Surface Boundary Layer |
| TKE | Turbulent Kinetic Energy |
| WMBL | Well-Mixed Boundary Layer |

## Appendix B. The one-dimensional GOTM model and the $k-\epsilon$-SG parameterization.

Throughout this manuscript we rely on one-dimensional ocean surface boundary layer (OSBL) simulations. We briefly review the details of the models employed here. In each case a linear equation of state with a constant thermal expansion coefficient is used. We do not include the effect of salinity since we are more generally concerned with the density, regardless of its constituents.

### *B1. GOTM And the $k-\epsilon$ approach*

The General Ocean Turbulence Model (GOTM, *gotm.net*) is used for all simulations with the $k-\epsilon$ parameterization here. The GOTM driver is implemented with a Crank-Nicholson time scheme capable of full forward and backward Euler methods (see Umlauf et al., 2005). For all simulations presented here using GOTM we choose a Crank-Nicholson implicitness factor of 0.5. $k-\epsilon$ model coefficients are chosen as the defaults in GOTM. We choose the stability functions of Schumann and Gerz (1995) based on findings of (Peters and Baumert, 2007; Ilıcak et al., 2008). We refer the reader to these documents for significantly more details on the model formulation.

### *B2. MOM6 And the JHL and ePBL approaches*

The 6th version of the Modular Ocean Model (Adcroft et al., 2018) is used for all simulations using JHL and ePBL. A single column model implementation of this model is emulated through a periodic 2x2 domain with homogenous surface forcing. In all simulations a full implicit time-step scheme is used to solve the diffusion equations. We refer the reader to *mom6.readthedocs.io* and the provided github address for further details on the model formulation.

## Appendix C. TKE Storage vs Mixing

Here we show the time-scale on which the steady-state TKE assumption is applicable. These experiments are all conducted using the $k-\epsilon$ parameterization with the same approach as described in B.1. We investigate the time dependence of two terms from the integrated TKE budget to test this approximation:

$$\underbrace{\int_{-H_{bl}}^{0}\frac{\partial k}{\partial t}dz}_{\text{Storage}} = \int_{z'}^{0}\frac{\partial}{\partial z}\left(\frac{K_M}{\sigma_k}\frac{\partial k}{\partial z}\right)dz + \int_{z'}^{0}K_M M^2 dz - \int_{z'}^{0}K_\phi \underbrace{\max(N^2,0)}_{\text{Mixing}}dz - \int_{z'}^{0}K_\phi \min(N^2,0)dz - \int_{z'}^{0}(\epsilon))dz. \tag{C.1}$$

The term we seek to parameterize in ePBL is the TKE that contributes to buoyancy mixing (conversion to potential energy, third term from right for $K_\phi N^2 > 0$). In order to determine that this term is larger than the storage (LHS in the TKE budget), we plot these two terms over the first 12 hours after forcing is applied. For this experiment we conduct 6 simulations. We vary the forcing to investigate weak shear-driven (0.05 N $m^{-2}$), strong shear-driven (0.2 N $m^{-2}$), and shear and buoyancy driven (0.05 N $m^{-2}$ and -100 W $m^{-2}$) cases. We conduct each case with both equatorial and high-latitude (60°) Coriolis parameters. Comparing the magnitude of the mixing component of the TKE budget to the time storage term we see that the mixing term overtakes the storage term for all scenarios beginning at two hours of simulation. The production and dissipation terms are not shown but are significantly larger than either term investigated here. Therefore, we conclude that using a steady-state TKE budget in our model is likely to be reasonable as long as we are interested in processes with timescales longer than one to two hours.

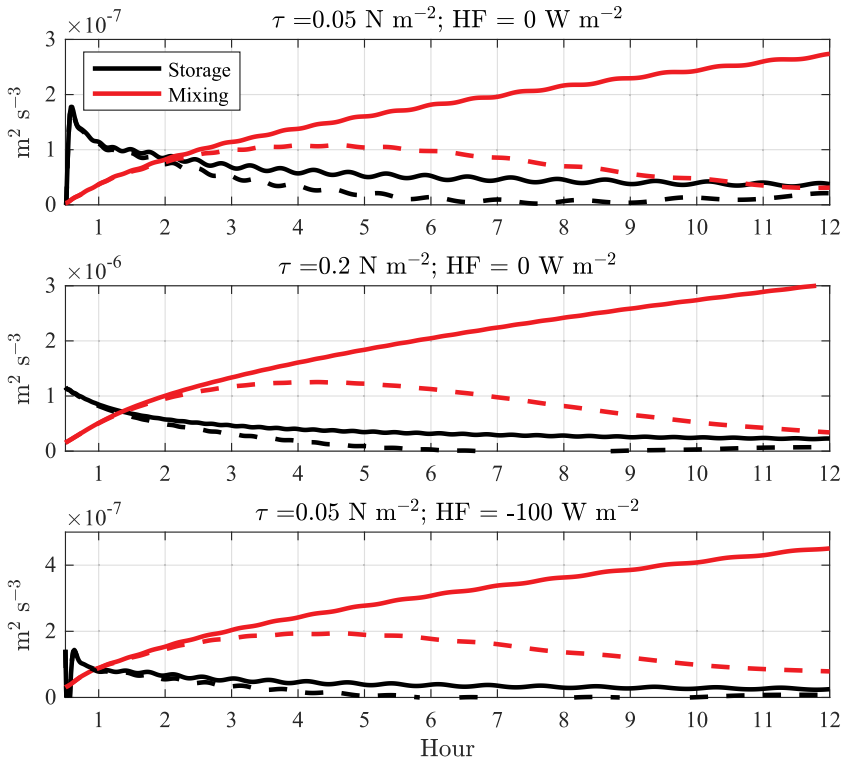


**Fig. C1.** Integrated TKE storage (black) and TKE consumed by mixing (red) (see Eq. (C.1)) from 12 hours of column model simulations using $k-\epsilon$ mixing. The TKE consumed by mixing is larger than the storage for times longer than two hours in all circumstances. The solid lines represent equatorial simulations and the dashed lines are run at a latitude of 60° N. Wind-stress, and surface heat flux are given by the panel titles. (For interpretation of the references to colour in this figure legend, the reader is referred to the web version of this article.)

## References


Adcroft, A., Hallberg, R.W., the MOM6 team, 2018. MOM6. Model Source and Documentation. . github.com/NOAA-GFDL/MOM6-examples/wiki.

Bachman, S.D., Fox-Kemper, B., Taylor, J.R., Thomas, L.N., 2017. Parameterization of frontal symmetric instabilities. I: theory for resolved fronts. Ocean Modell. 109, 72–95.

Belcher, S.E., Grant, A.L.M., Hanley, K.E., Fox-Kemper, B., Van Roekel, L., Sullivan, P.P., Large, W.G., Brown, A., Hines, A., Calvert, D., Rutgersson, A., Pettersson, H., Bidlot, J.-R., Janssen, P.A.E.M., Polton, J.A., 2012. A global perspective on Langmuir turbulence in the ocean surface boundary layer. Geophys. Res. Lett. 39 (L18605), 1–9.

Bleck, R., 2002. An oceanic general circulation model framed in hybrid isopycnic-cartesian coordinates. Ocean Modell. 37, 55–88.

Boussinesq, J., 1877. Essai sur la théorie des eaux courantes. Mémoires présentés par divers savants á l'Académie des Sci. 23, 1–680.

Bueti, M., Ginis, I., Rothstein, L.M., Griffies, S.M., 2014. Tropical cyclone-induced thermocline warming and its regional and global impacts. J. Clim. 27, 6978–6999.

Burchard, H., Baumert, H., 1995. On the performance of a mixed-layer model based on the $k-\epsilon$ turbulence closure. J. Geophys. Res. 100 (C5), 8523–8540.

Burchard, H., Bolding, K., 2001. Comparative analysis of four second-moment turbulence closure models for the oceanic mixed layer. J. Phys. Oceanogr. 31, 1943–1968.

Burchard, H., Craig, P.D., Gemmrich, J.R., van Harden, H., Mathieu, P.P., Meier, H.E.M., Smith, W.A.M.N., Prandke, H., Rippeth, T.P., Skyllingstad, E.D., Smyth, W.D., Welsh, D.J.S., Wijesekera, H.W., 2008. Obervational and numerical modeling methods for quantifying coastal ocean turbulence and mixing. Prog. Oceanogr. 76, 399–442.

Burchard, H., Peterson, O., Rippeth, T.P., 1998. Comparing the performance of the Mellor-Yamada and the $k-\epsilon$ two-equation turbulence models. J. Geophys. Res. 103 (C5), 10543–10554.

Canuto, V.M., Howard, A.M., Cheng, Y., Dubovikov, M.S., 2001. Ocean turbulence. Part I: one-point closure model of momentum and heat vertical diffusivities. J. Phys. Oceanogr. 31, 1413–1426.

Carson, D.J., 1973. The development of a dry inversion capped convectively unstable boundary layer. Q. J. R. Meteorolog. Soc. 99, 450–467.

Caughey, S.J., Palmer, S.G., 1979. Some aspects of turbulence structure through the depth of the convective boundary layer. Q. J. R. Meteorolog. Soc. 105, 811–827.

Craig, P.D., Banner, M.L., 1994. Modeling wave-enhanced turbulence in the ocean surface layer. J. Phys. Oceanogr. 24, 2546–2559.

Craik, A.D.D., Leibovich, S., 1976. A rational model for Langmuir circulations. J. Fluid Mech. 73 (3), 401–426.

D'Alessio, J.S.D., Abdella, K., McFarlane, N.A., 1998. A new second-order turbulence closure scheme for modeling the oceanic mixed layer. J. Phys. Oceanogr. 28, 1624–1641.

D'Asaro, E., Lee, C., Rainville, L., Harcourt, R., Thomas, L., 2011. Enhanced turbulence and energy dissipation at ocean fronts. Science 332, 318–322.

D'Asaro, E.A., Thomson, J., Shcherbina, A.Y., Harcourt, R.R., Cronin, M.F., Hemer, M.A., Fox-Kemper, B., 2014. Quantifying upper ocean turbulence driven by surface waves. Geophys. Res. Lett. 41, 1–6.

Deardorff, J.W., 1983. A multi-limit mixed-layer entrainment formulation. J. Phys. Oceanogr. 13, 988–1002.

Ellison, T.H., Turner, J.S., 1959. Turbulent entrainment in stratified flows. J. Fluid Mech. 6, 423–448.

Fan, Y., Griffies, S.M., 2014. Impacts of parameterized Langmuir turbulence and non-breaking wave mixing in global climate simulations. J. Clim. 27, 4752–4775.

Fox-Kemper, B., Danabasoglu, G., Ferrari, R., Griffies, S.M., Hallberg, R.W., Holland, M.M., Maltrud, M.E., Peacock, S.L., Samuels, B.L., 2011. Parameterization of mixed layer eddies. III: implementation and impact in global ocean climate simulations. Ocean Modell. 39 (1–2), 61–78.

Galperin, B., Kantha, L.H., Hassid, S., Rosati, A., 1988. A quasi-equilibrium turbulent kinetic energy model for geophysical flows. J. Atmos. Sci. 45 (1), 55–62.

Garwood, R.W., 1977. An oceanic mixed layer model capable of simulating cyclic states. J. Phys. Oceanogr. 7, 455–468.

Gaspar, P., 1988. Modeling of the seasonal cycle of the upper ocean. J. Phys. Oceanogr. 18, 161–180.

Gaspar, P., Grégoris, Y., Lefevre, J.-M., 1990. A simple eddy kinetic energy model for simulations of the oceanic vertical mixing: tests at Station Papa and long-term upper ocean study site. J. Geophys. Res. 95 (C9), 16179–16193.

Griffies, S.M., Danabasoglu, G., Durack, P.J., et. al, 2016. OMIP Contribution to CMIP6: experimental and diagnostic protocol for the physical component of the ocean model intercomparison project. Geosci. Model Dev. 9, 3231–3296.

Hallberg, R.W., 2003. The suitability of large-scale ocean models for adapting parameterizations of boundary mixing and a description of a refined bulk mixed layer model. Near-Boundary Processes and Their Parameterization. Proceedings of the 13th Aha Huliko'a Hawaiian Winter Workshop. University of Hawai'i at Mānoa, pp. 187–203.

Harcourt, R.R., 2013. A second-moment closure model of Langmuir turbulence. J. Phys. Oceanogr. 43, 673–697.

Harcourt, R.R., 2015. An improved second-moment closure model of Langmuir turbulence. J. Phys. Oceanogr. 45, 84–103.

Ilıcak, M., Özgökmen, T.M., Peters, H., Baumert, H.Z., Iskandarani, M., 2008. Performance of two-equation turbulence closures in three-dimensional simulations of the Red Sea overflow. Ocean Modell. 24, 122–139.

Jackson, L., Hallberg, R., Legg, S., 2008. A parameterization of shear-driven turbulence for ocean climate models. J. Phys. Oceanogr. 38, 1033–1053.

Kantha, L.H., 2004. The length scale equation in turbulence models. Nonlinear Process Geophys. 11, 83–97.

Kantha, L.H., Clayson, C.A., 1994. An improved mixed layer model for geophysical

applications. J. Geophys. Res. 99, 25235–25266.
Kantha, L.H., Clayson, C.A., 2004. On the effect of surface gravity waves on mixing in the oceanic mixed layer. Ocean Modell. 6, 101–124.
Kolmogorov, A.N., 1942. The equation of turbulent motion in an incompressible fluid. Izv. Akad. Nauk SSSR Ser. Fiz. 6, 56–58.
Kraus, E.B., Turner, J.S., 1967. A one-dimensional model of the seasonal thermocline II. The general theory and its consequences. Tellus 19, 98–105.
Large, W.G., McWilliams, J.C., Doney, S.C., 1994. Oceanic vertical mixing: a review and a model with a nonlocal boundary layer parameterization. Rev. Geophys. 32 (4), 363–403.
Li, Q., Webb, A., Fox-Kemper, B., Craig, A., Danabasoglu, G., Large, W.G., Vertenstein, M., 2016. Langmuir mixing effects on global climate: WAVEWATCH III in CESM. Ocean Modell. 103, 145–160.
McWilliams, J.C., Huckle, E., Liang, J.-H., Sullivan, P.P., 2012. The wavy Ekman layer: Langmuir circulations, breaking waves, and Reynolds stress. J. Phys. Oceanogr. 42, 1793–1816.
McWilliams, J.C., Sullivan, P.P., Moeng, C.H., 1997. Langmuir turbulence in the ocean. J. Fluid Mech. 334, 1–30.
Mellor, G.L., Yamada, T., 1974. A hierarchy of turbulence closure models for planetary boundary layers. J. Atmos. Sci. 31, 1791–1806.
Mellor, G.L., Yamada, T., 1982. Development of a turbulence closure model for geophysical fluid problems. Rev. Geophys. Space Phys. 20 (4), 851–875.
Melville, W.K., 1996. The role of surface-wave breaking in air-sea interaction. Annu. Rev. Fluid Mech. 28, 279–321.
Moeng, C.H., Sullivan, P.P., 1994. A comparison of shear and buoyancy-driven planetary boundary layer flows. J. Atmos. Sci. 51, 999–1022.
Moum, J.N., Smyth, W.D., 2001. Upper ocean mixing. Encyclopedia of Ocean Sciences. Academic Press, pp. 3093–3100.
Niiler, P.P., Kraus, E.B., 1977. One-dimensional models of the upper ocean. In: Kraus, E.B. (Ed.), Modelling and Prediction of the Upper Layers of the Ocean. Pergamon Press, pp. 143–172.
Noh, Y., Hoh, G., Raasch, S., 2010. Examination of the mixed layer deepening process during convection using LES. J. Phys. Oceanogr. 40, 2189–2195.
Noh, Y., Min, S., Raasch, S., 2004. Large eddy simulation of the ocean mixed layer: the effects of wave breaking and Langmuir circulation. J. Phys. Oceanogr. 34, 720–735.
Oberhuber, J.M., 1993. Simulation of the atlantic circulation with a coupled sea ice-mixed layer-isopycnal general circulation model. part I: model description. J. Phys. Oceanogr. 23, 808–829.
Pacanowski, R.C., Philander, S.G.H., 1981. Parameterization of vertical mixing in numerical models of tropical oceans. J. Phys. Oceanogr. 11, 83–89.
Peters, H., Baumert, H.Z., 2007. Validating a turbulence closure against estuarine microstructure measurements. Ocean Modell. 19, 183–203.
Pollard, R.T., Rhines, P.B., Thompson, R.O.R.Y., 1972. The deepening of the wind-mixed layer. Geophys. Fluid Dyn. 4 (1), 381–404.
Reffray, G., Bourdalle-Badie, R., Calone, C., 2015. Modelling turbulent vertical mixing sensitivity using a 1-d version of NEMO. Geosci. Model Dev. 8, 69–86.
Reichl, B.G., Wang, D., Hara, T., Ginis, I., Kukulka, T., 2016. Langmuir turbulence parameterization in tropical cyclone conditions. J. Phys. Oceanogr. 46, 863–886.
Rodhe, J., 1991. Wind mixing in a turbulent surface layer in the presence of a horizontal density gradient. J. Phys. Oceanogr. 21, 1080–1083.
Rodi, W., 1987. Examples of calculation methods for flow and mixing in stratified fluids. J. Geophys. Res. 92 (C5), 5305–5328.
Schmitt, F.G., 2007. About Boussinesq's turbulent viscosity hypothesis: historical remarks and a direct evaluation of its validity. C. R. Macanique 335, 617–627.
Schumann, U., Gerz, T., 1995. Turbulent mixing in stably stratified shear flows. J. Appl. Meteorol. 34, 33–48.
Skyllingstad, E.D., Denbo, D.W., 1995. An ocean large-eddy simulation of Langmuir circulations and convection in the surface mixed layer. J. Geophys. Res. 100 (C5), 8501–8522.
Skyllingstad, E.D., Smyth, W.D., Crawford, G.B., 2000. Resonant wind-driven mixing in the ocean boundary layer. J. Phys. Oceanogr. 30, 1866–1890.
Soloviev, A., Lukas, R., 2013. The-Near surface layer of the ocean: Structure, dynamics, and applications. Springer Science and Business Media.
Stull, R.B., 1976. The energetics of entrainment across a density interface. J. Atmos. Sci. 33 (1260–1267).
Sullivan, P.P., McWilliams, J.C., Melville, W.K., 2007. Surface gravity wave effects in the oceanic boundary layer: large-eddy simulation with vortex force and stochastic breakers. J. Fluid Mech. 593, 405–452.
Terray, E.A., Donelan, M.A., Agrawal, Y.C., Drennan, W.M., Kahma, K.K., Williams III, A.J., Hwang, P.A., Kitaigorodskii, S.A., 1996. Estimates of kinetic energy dissipation under breaking waves. J. Phys. Oceanogr. 26 (792–807).
Thomas, L., Ferrari, R., 2008. Friction, frontogenesis, and the stratification of the surface mixed layer. J. Phys. Oceanogr. 38, 2501–2518.
Thompson, L., Kelly, K.A., Darr, D., Hallberg, R., 2002. Buoyancy and mixed layer effects on the sea surface height response in an isopycnal model of the north pacific. J. Phys. Oceanogr. 32, 3657–3670.
Umlauf, L., 2009. The description of mixing in stratified layers without shear in large-scale ocean models. J. Phys. Oceanogr. 39, 3032–3039.
Umlauf, L., Burchard, H., 2003. A generic length-scale equation for geophysical turbulence models. J. Mar. Syst. 61 (2), 235–265.
Umlauf, L., Burchard, H., 2005. Second-order turbulence closure models for geophysical boundary layers. A review of recent work. Cont. Shelf Res. 25 (7–8), 795–827.
Umlauf, L., Burchard., H., Bolding, K., 2005. GOTM - Scientific Documentation. Technical Report. Leiniz-Institute for Baltic Sea Research Marine Science.
Van Roekel, L., Adcroft, A.J., Danabasoglu, G., Griffies, S.M., Kauffman, B., Large, W.G., Levy, M., Reichl, B.G., Ringler, T., Schmidt, M., 2018. The KPP boundary layer scheme for the ocean: revisiting its formulation and benchmarking one-dimensional simulations relative to LES. J. Adv. Model. Earth Syst. In press..
Warner, J.C., Sherwood, C.R., Arango, H.G., Signell, R.P., 2005. Performance of four turbulence closure models implemented using a generic length scale method. Ocean Modell. 8, 81–113.
Wilcox, D.C., 1988. Reassessment of the scale-determining equation for advanced turbulence models. AIAA J. 26 (11), 1299–1310.
Zilitinkevich, S., Mironov, D., 1996. A multi-limit formulation for the equilibrium depth of a stably stratified boundary layer. Boundary Layer Meteorol. 81, 325–351.